2020

Inertial Orbit Estimation Using Multiple Space Based Observers: A New Measurement Model

James Hippelheuser
University of Central Florida

INERTIAL ORBIT ESTIMATION USING MULTIPLE SPACE BASED OBSERVERS: A NEW MEASUREMENT MODEL

by

JAMES EDWARD HIPPELHEUSER JR.
B.S. University of Central Florida, 2011

A thesis submitted in partial fulfilment of the requirements
for the degree of Master of Science
in the Department of Mechanical and Aerospace Engineering
in the College of Engineering and Computer Science
at the University of Central Florida
Orlando, Florida

Spring Term
2020

Major Professor: Tarek A. Elgohary

ABSTRACT

Presented within this work is a new method for inertial orbit estimation of an object, either known or unknown, adaptable to a network of low-cost observation satellites. The observation satellites would only require a monocular camera for line of sight measurements. Using the line of sight measurements of each observer, a pair of orthogonal geometric planes that intersect both the observation satellite and the target are created. The intersection of the two planes in the inertial frame defines the new measurement model that is implemented with multiple observation nodes. Total system observability is analyzed and the instantaneous (per node) observability is used to remove "bad" measurements from the system. The measurement model is used in an extended Kalman filter framework and the measurement noise nonlinear transformation is addressed. Three cases are presented; first, the minimum number of required observation nodes to produce accurate results if determined. Then, a smaller number of observation nodes is analyzed to highlight the use of the instantaneous observability and its deleterious effect on the filter performance. Finally, the method is expanded out to multiple observation satellites in a constellation. For all cases, the results show that this method is capable of producing accurate orbit estimation that converges in a short time.

I would like to dedicate this to my parents, Jim and Marijean, my sister, Katie, and to Amanda for their love and support.

ACKNOWLEDGMENTS

I would like to thank my advisor, Dr. Tarek Elgohary, for his support and guidance throughout the last year. I would also like to thank Dr. Jaydeep Mukherjee from NASA Florida Space Grant Consortium for providing funding for the work presented within.

TABLE OF CONTENTS

LIST OF FIGURES

LIST OF TABLES

CHAPTER 1: INTRODUCTION

Currently, the task of performing orbit determination is mainly accomplished by a series of ground-based optical and radar observation stations. These ground-based stations can be limited by various atmospheric conditions, including weather. In the case of the optical observation stations, they can only be utilized during night time hours and are effected by light pollution. With the ever increasing number of space flight operations and the limitations of ground-based observers, a gap in coverage begins to emerge. This gap can be filled with a network of low-cost observation satellite nodes, Figure 1.1, that are capable of providing accurate and highly efficient real-time orbit estimation of satellites, spacecraft, and other unknown objects.

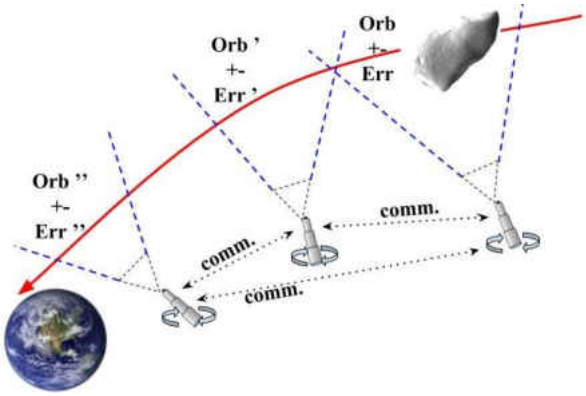

Figure 1.1: Illustration of a network of observation satellites.

With the expansion of both private and commercial space flights, autonomous rendezvous and on-orbit servicing could benefit the most from having such a network in place [1]–[4]. Furthermore, another application to benefit would be operations involving space debris tracking and removal. Currently it is believed that the number of debris in Earth orbit is approximately 500,000 [5] and exponentially increasing due to collisions [6]. According to NASA planetary defense program office, only a fraction of the larger Near Earth Objects (NEOs) are tracked and classified due to the

limitations of ground-based observers. When combined with the current network of ground based observations, a network of observation satellites has the potential of improving the tracking and identification of NEOs [7].

Literature Review

The literature of orbit determination and estimation is rich with several seminal contributions that date back to Gauss and Laplace. Early angles-only initial orbit determination (IOD) of Gauss [8] and Laplace [9] relied on ground based angle measurements to determine the orbit of celestial bodies. With the advent of space flight, iterative methods have been proposed, e.g. the Double-r method [10] and the Gooding method [11]. In general, IOD is used to provide an initial guess for other estimation and filtering techniques. A comprehensive comparison of widely used IOD methods is presented in [12]. Nonlinear least squares, e.g. Gauss least squares differential correction (GLSDC), is also capable of providing accurate orbit determination using a variety of measurement methods [13]. A multitude of filtering techniques have also been studied in the literature for Earth-based and space-based measurement models. A space-based angles-only orbit estimation approach using an extended Kalman filter (EKF) formulation in spherical coordinates is studied in [14]. The measurement model and the dynamics are transformed into a spherical coordinate system and the results are compared with the EKF implementation in Cartesian coordinates. Several other works focused on comparing the performance of different estimation techniques for various measurement models [13], [15]–[17]. The unscented Kalman filter (UKF) and the EKF have been extensively studied in these works highlighting there advantages and limitations as a result of the measurements sampling time, the measurement model, the sensitivity towards the initial covariance, the accuracy and the computational time. For example, Teixeira, Santillo, Erwin, *et al.* [16] used a range-only and a range, azimuth and elevation space-based measurement models to com-

pare the EKF and the UKF while varying the sampling time. Their results show that the UKF has better convergence characteristics with sparser sampling whereas the EKF has an advantage in computational efficiency.

There are a variety of measurement methods available to perform orbit determination [18]. Some examples of these methods include azimuth and elevation angles and range measurements, and azimuth and elevation angles only measurements. Azimuth and elevation angles and range measurements can be acquired using either radar or LiDAR [19]–[22]. Angles only measurements can simply be acquired by observing an object using a telescope or a monocular camera [23]–[29]. Unfortunately, the use of angles-only measurements for space-based orbit determination has proven challenging in the past. It has mainly been proposed for orbit estimation during single purpose, close proximity missions. Because of the close proximity, most studies have been mainly focused on relative orbit dynamics. Using the linearized Clohessy-Wiltshire-Hill (CWH) equations for relative motion with a single observer, Woffinden and Geller [30] showed that the system is non-observable due to the absence of range measurements.

To overcome the observability problem, studies have shown that when using higher order or the full nonlinear relative dynamics, the system can become observable [23]–[25]. Butcher, Wang, and Lovell [23] verified that when using the first order CWH equations with angles only measurements, the system is non-observable. They then went on to perform analysis by including the second and third order terms of the Taylor expansion as well as the full nonlinear relative dynamic model. They were able to show that with each higher order term there was an increase in observability and a decrease in error and that the third order expansion performed equally to the full nonlinear dynamics. Others have approached this problem by providing a second measurement perspective during sequential measurements, showing that by applying a specific control input, either translational or rotational, the system will become observable for select scenarios [25]–[27]. It has also been shown that it is possible to come up with an optimal control to maximize the observability

while minimizing the number of maneuvers during a rendezvous scenario [28], [29]. Besides not being observable at all time, this approach also has the drawback of requiring the continuous use of propellant, limiting its service life. Geller and Klein [31] showed that these results can be produced without the control input, simply by offsetting the imaging camera and taking that offset into account in the system dynamics. However, there were still several instances where the system was non-observable.

Another approach to using line of sight measurements has been to introduce a second monocular camera on a secondary or deputy spacecraft [32], [33]. With this approach, in order to use relative motion dynamics, the measurements of the secondary spacecraft have to be a function of the states of the primary spacecraft. Wang, Zhang, Zhou, *et al.* [34] proposed a similar method of using a secondary spacecraft but in inertial frame. However, it required that the ranging information between the primary and secondary spacecraft to be available. In Li, Wang, and Zheng [35], using only dual-point of view observations, it was shown to be capable of orbit determination in the inertial frame without the need for any range information. It was also shown that the accuracy of the orbit determination was higher when the orbit of the observer and the placement of the camera on the observers were optimized to maximize exposure of the target to the observers.

Objectives

The objectives of this thesis are to:

- Develop a measurement model that is capable of accurately performing orbit estimation using only angle measurements from multiple independent observation nodes.
- Validate the measurement models ability to perform orbit estimation on an unknown target in orbit.

Outline

Chapter 2 presents the derivation of the new measurement model, how the estimation scheme was implemented, and observability analysis performed.

Chapter 3 discuses the numerical simulation used to validate the new measurement model and analyzes the results.

Chapter 4 summarizes the conclusions of this thesis as well as future work to be explored.

CHAPTER 2: MULTI-NODE ORBIT ESTIMATION

Measurement Model

The proposed measurement model revolves around the facts that any line in three dimensional space can be defined as the intersection of two planes, Figure 2.1A, and that any point is defined as the intersection of two lines [36], Figure 2.1B. To define a plane, the essential ingredients are the surface normal of the plane, $[n_x \;\; n_y \;\; n_z]$, and a known point on the plane, $[X \;\; Y \;\; Z]$. Any other point on the plane, $[x \;\; y \;\; z]$, can be expressed as

$$\begin{bmatrix} n_x & n_y & n_z \end{bmatrix} \begin{bmatrix} x & y & z \end{bmatrix}^T = n_x X + n_y Y + n_z Z \tag{2.1}$$

When using planes to define a line, a surface normal from each of the intersecting planes, $[n_{x_1} \;\; n_{y_1} \;\; n_{z_1}]$ and $[n_{x_2} \;\; n_{y_2} \;\; n_{z_2}]$, and a common known point, $[X \;\; Y \;\; Z]$, are required. Any point on the line is expressed as

$$\begin{bmatrix} n_{x_1} & n_{y_1} & n_{z_1} \\ n_{x_2} & n_{y_2} & n_{z_2} \end{bmatrix} \begin{bmatrix} x & y & z \end{bmatrix}^T = \begin{bmatrix} n_{x_1} X + n_{y_1} Y + n_{z_1} Z \\ n_{x_2} X + n_{y_2} Y + n_{z_2} Z \end{bmatrix} \tag{2.2}$$

The point of two intersecting lines can then be expressed as

$$\begin{bmatrix} n_{x_{1,1}} & n_{y_{1,1}} & n_{z_{1,1}} \\ n_{x_{1,2}} & n_{y_{1,2}} & n_{z_{1,2}} \\ n_{x_{2,1}} & n_{y_{2,1}} & n_{z_{2,1}} \\ n_{x_{2,2}} & n_{y_{2,2}} & n_{z_{2,2}} \end{bmatrix} \begin{bmatrix} x & y & z \end{bmatrix}^T = \begin{bmatrix} n_{x_{1,1}} X_1 + n_{y_{1,1}} Y_1 + n_{z_{1,1}} Z_1 \\ n_{x_{1,2}} X_1 + n_{y_{1,2}} Y_1 + n_{z_{1,2}} Z_1 \\ n_{x_{2,1}} X_2 + n_{y_{2,1}} Y_2 + n_{z_{2,1}} Z_2 \\ n_{x_{2,2}} X_2 + n_{y_{2,2}} Y_2 + n_{z_{2,2}} Z_2 \end{bmatrix} \tag{2.3}$$

Assuming the form,

$$A\mathbf{x} = b \tag{2.4}$$

the solution for the point of intersection is

$$\mathbf{x} = (A^T A)^{-1} A^T b \tag{2.5}$$

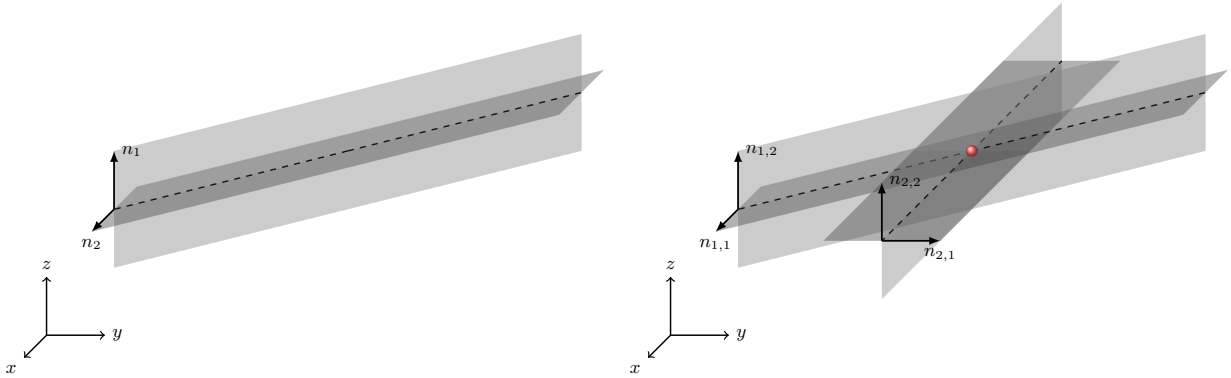

(A) (B)

Figure 2.1: (A) Two intersecting planes creating a line. (B) Two intersecting lines, represented by planes, creating a point.

In the case of multiple satellites, for each observation node, starting with the monocular camera, two angle measurements, elevation (El) and azimuth (Az), are measured as shown in Figure 2.2. With these angle measurements, a line of sight unit vector ($\mathbf{L\hat{O}S}$) can be created, pointing from the observation node to the target in the body frame of the observation node.

$$\mathbf{L\hat{O}S}^{Body}_{Obs \to Tar} = \begin{bmatrix} \cos El \sin Az \\ \cos El \cos Az \\ \sin El \end{bmatrix} \tag{2.6}$$

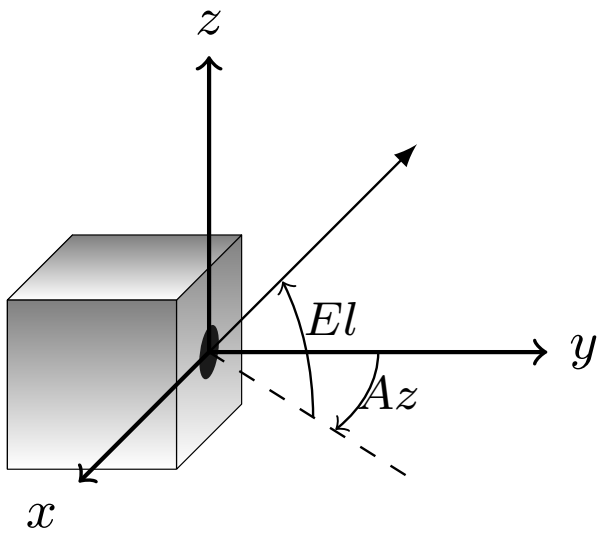

Figure 2.2: Angle measurements

The $\mathbf{L\hat{O}S}$ can be rotated from the body frame to the local vertical, local horizontal (LVLH) frame of the observation node,

$$\mathbf{L\hat{O}S}^{LVLH}_{Obs\rightarrow Tar} = \begin{bmatrix} 1 & 0 & 0 \\ 0 & \cos\phi & -\sin\phi \\ 0 & \sin\phi & \cos\phi \end{bmatrix} \begin{bmatrix} \cos\theta & 0 & \sin\theta \\ 0 & 1 & 0 \\ -\sin\theta & 0 & \cos\theta \end{bmatrix} \begin{bmatrix} \cos\psi & -\sin\psi & 0 \\ \sin\psi & \cos\psi & 0 \\ 0 & 0 & 1 \end{bmatrix} \mathbf{L\hat{O}S}^{Body}_{Obs\rightarrow Tar} \quad (2.7)$$

Where ϕ, θ, and ψ are the Euler angles, Figure 2.3A, roll, pitch, and yaw of the observation node, respectively. $\mathbf{L\hat{O}S}$ can then be rotated from the LVLH frame of the observation node to the ECI

frame, Figure 2.3B,

$$\mathbf{L\hat{O}S}^{ECI}_{Obs\rightarrow Tar} = \begin{bmatrix} \cos\Theta & -\sin\Theta & 0 \\ \sin\Theta & \cos\Theta & 0 \\ 0 & 0 & 1 \end{bmatrix} \begin{bmatrix} 1 & 0 & 0 \\ 0 & \cos i & -\sin i \\ 0 & \sin i & \cos i \end{bmatrix} \begin{bmatrix} \cos\Omega & -\sin\Omega & 0 \\ \sin\Omega & \cos\Omega & 0 \\ 0 & 0 & 1 \end{bmatrix} \mathbf{L\hat{O}S}^{LVLH}_{Obs\rightarrow Tar} \quad (2.8)$$

where, i is the inclination angle, Ω is the longitude of the ascending node, and Θ is the true longitude defined as the sum of the true anomaly and the argument of periapsis, all for the observation node. From here on, unless otherwise stated, all vectors and measurements are assumed to be in the ECI frame.

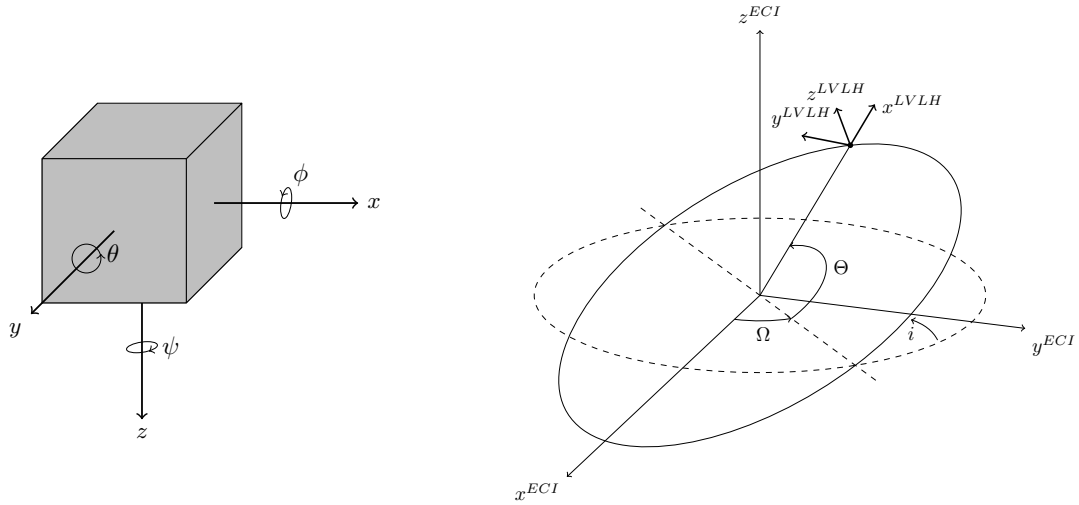

(A) (B)

Figure 2.3: (A) Euler angles. (B) LVLH coordinate system.

With multiple observation nodes observing a single target, multiple $\mathbf{L\hat{O}S}$ vectors are created as shown in Figure 2.4 for N number of observation nodes. From Figure 2.4, the $\mathbf{L\hat{O}S}$ from each observation node to the target can be represented as,

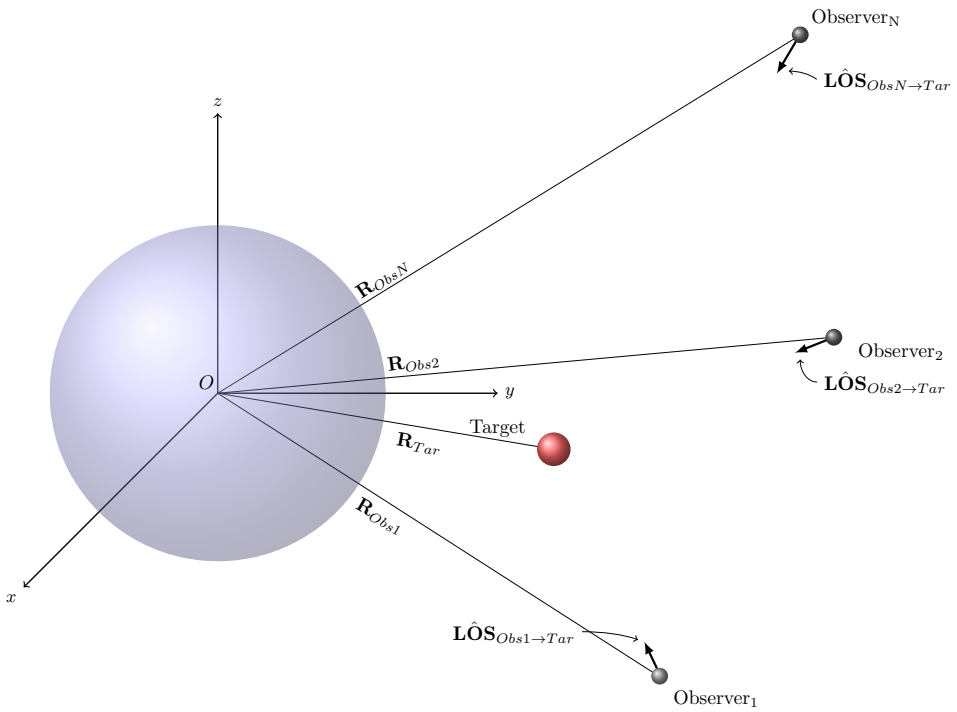

Figure 2.4: Line of sight vectors for N observation nodes.

$$
\begin{aligned}
\hat{\mathbf{LOS}}_{Obs1\rightarrow Tar} &= \begin{bmatrix} \hat{x}_{Obs1\rightarrow Tar} & \hat{y}_{Obs1\rightarrow Tar} & \hat{z}_{Obs1\rightarrow Tar} \end{bmatrix}^T \\
\hat{\mathbf{LOS}}_{Obs2\rightarrow Tar} &= \begin{bmatrix} \hat{x}_{Obs2\rightarrow Tar} & \hat{y}_{Obs2\rightarrow Tar} & \hat{z}_{Obs2\rightarrow Tar} \end{bmatrix}^T \\
&\vdots \\
\hat{\mathbf{LOS}}_{ObsN\rightarrow Tar} &= \begin{bmatrix} \hat{x}_{ObsN\rightarrow Tar} & \hat{y}_{ObsN\rightarrow Tar} & \hat{z}_{ObsN\rightarrow Tar} \end{bmatrix}^T
\end{aligned}
\tag{2.9}
$$

The state vector of the target is given by,

$$\mathbf{X}_{Tar} = \begin{bmatrix} \mathbf{R}_{Tar} & \mathbf{V}_{Tar} \end{bmatrix}^T = \begin{bmatrix} x_{Tar} & y_{Tar} & z_{Tar} & \dot{x}_{Tar} & \dot{y}_{Tar} & \dot{z}_{Tar} \end{bmatrix}^T \tag{2.10}$$

and the state vector for each observation node is,

$$\begin{aligned} \mathbf{X}_{Obs1} &= \begin{bmatrix} \mathbf{R}_{Obs1} & \mathbf{V}_{Obs1} \end{bmatrix}^T = \begin{bmatrix} x_{Obs1} & y_{Obs1} & z_{Obs1} & \dot{x}_{Obs1} & \dot{y}_{Obs1} & \dot{z}_{Obs1} \end{bmatrix}^T \\ \mathbf{X}_{Obs2} &= \begin{bmatrix} \mathbf{R}_{Obs2} & \mathbf{V}_{Obs2} \end{bmatrix}^T = \begin{bmatrix} x_{Obs2} & y_{Obs2} & z_{Obs2} & \dot{x}_{Obs2} & \dot{y}_{Obs2} & \dot{z}_{Obs2} \end{bmatrix}^T \\ &\vdots \\ \mathbf{X}_{ObsN} &= \begin{bmatrix} \mathbf{R}_{ObsN} & \mathbf{V}_{ObsN} \end{bmatrix}^T = \begin{bmatrix} x_{ObsN} & y_{ObsN} & z_{ObsN} & \dot{x}_{ObsN} & \dot{y}_{ObsN} & \dot{z}_{ObsN} \end{bmatrix}^T \end{aligned} \tag{2.11}$$

Using the position of the observation nodes, unit vectors from the observation nodes to the origin of the ECI frame are created,

$$\begin{aligned} \hat{\mathbf{R}}_{Obs1\to O} &= \frac{-\mathbf{R}_{Obs1}}{\|\mathbf{R}_{Obs1}\|} = \begin{bmatrix} \hat{x}_{Obs1\to O} & \hat{y}_{Obs1\to O} & \hat{z}_{Obs1\to O} \end{bmatrix}^T \\ \hat{\mathbf{R}}_{Obs2\to O} &= \frac{-\mathbf{R}_{Obs2}}{\|\mathbf{R}_{Obs2}\|} = \begin{bmatrix} \hat{x}_{Obs2\to O} & \hat{y}_{Obs2\to O} & \hat{z}_{Obs2\to O} \end{bmatrix}^T \\ &\vdots \\ \hat{\mathbf{R}}_{ObsN\to O} &= \frac{-\mathbf{R}_{ObsN}}{\|\mathbf{R}_{ObsN}\|} = \begin{bmatrix} \hat{x}_{ObsN\to O} & \hat{y}_{ObsN\to O} & \hat{z}_{ObsN\to O} \end{bmatrix}^T \end{aligned} \tag{2.12}$$

For each observation node, two planes are created that intersect both the observation node and the target as shown in Figure 2.5. For both planes, the position of the K^{th} observation node is used as

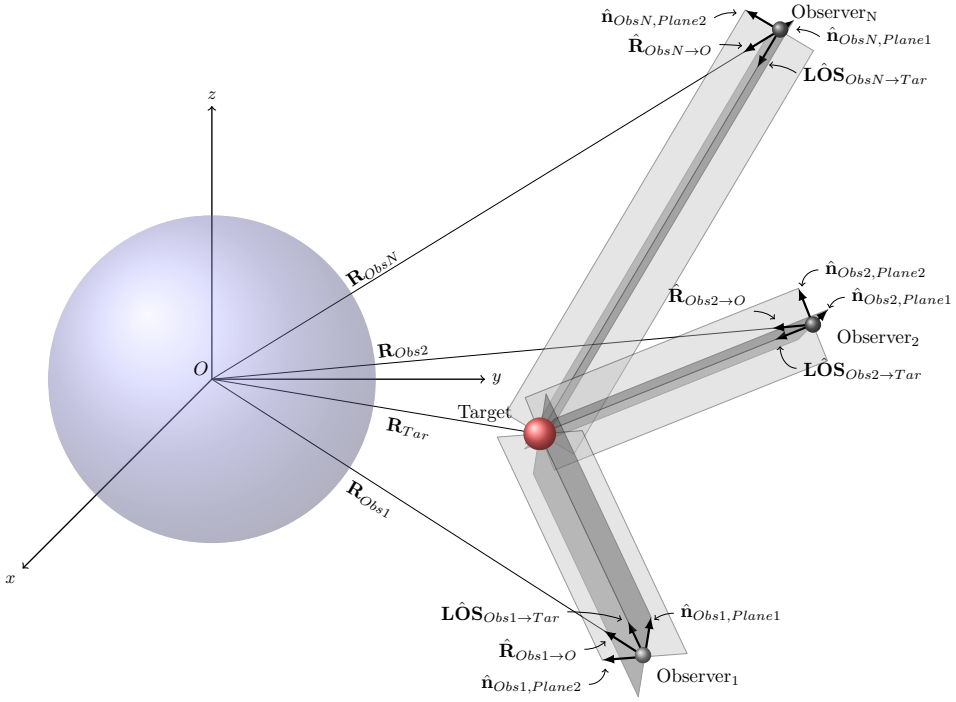

Figure 2.5: Geometric planes that intersect both the K^{th} observation node and the target.

the known point. The normal vector for the first plane is defined as the cross product of the $\hat{\mathbf{LOS}}$ in Equation 2.9, and the position unit vector in Equation 2.12

$$\hat{\mathbf{n}}_{ObsK,Plane1} = \hat{\mathbf{LOS}}_{ObsK\to Tar} \times \hat{\mathbf{R}}_{ObsK\to O} = \begin{bmatrix} \hat{x}_{ObsK,Plane1} & \hat{y}_{ObsK,Plane1} & \hat{z}_{ObsK,Plane1} \end{bmatrix}^T \tag{2.13}$$

From Equation 2.11 and Equation 2.13, the equation for the first plane, as function of the first normal vector and the K^{th} observer, is

$$\hat{x}_{ObsK,Plane1}(x - x_{ObsK}) + \hat{y}_{ObsK,Plane1}(y - y_{ObsK}) + \hat{z}_{ObsK,Plane1}(z - z_{ObsK}) = 0 \tag{2.14}$$

For the second plane, the normal vector is the cross product of the normal vector of the first plane, Equation 2.13 and the $\mathbf{L\hat{O}S}$, Equation 2.9,

$$\hat{\mathbf{n}}_{ObsK,Plane2} = \hat{\mathbf{n}}_{ObsK,Plane1} \times \mathbf{L\hat{O}S}_{ObsK \to Tar} = \begin{bmatrix} \hat{x}_{ObsK,Plane2} & \hat{y}_{ObsK,Plane2} & \hat{z}_{ObsK,Plane2} \end{bmatrix}^T \quad (2.15)$$

From Equation 2.11 and Equation 2.15, the equation for the second plane, as function of the second normal vector and the K^{th} observer, is

$$\hat{x}_{ObsK,Plane2}(x - x_{ObsK}) + \hat{y}_{ObsK,Plane2}(y - y_{ObsK}) + \hat{z}_{ObsK,Plane2}(z - z_{ObsK}) = 0 \quad (2.16)$$

In order to use the equations of each plane as a measurement model, the terms that contain the measurements, elevation (El) and azimuth (Az), have to be isolated to one side of the equation. The terms containing the measurements are the components of the normal vectors of each plane. To accomplish this, Equation 2.14 and Equation 2.16 are rearranged into the vector-matrix form,

$$\begin{bmatrix} \hat{x}_{ObsK,Plane1} & \hat{y}_{ObsK,Plane1} \\ \hat{x}_{ObsK,Plane2} & \hat{y}_{ObsK,Plane2} \end{bmatrix} \begin{bmatrix} (x - x_{ObsK}) \\ (y - y_{ObsK}) \end{bmatrix} + \begin{bmatrix} \hat{z}_{ObsK,Plane1} \\ \hat{z}_{ObsK,Plane2} \end{bmatrix} (z - z_{ObsK}) = 0 \quad (2.17)$$

Finally, Equation 2.17 can be rewritten as,

$$\begin{bmatrix} \hat{x}_{ObsK,Plane1} & \hat{y}_{ObsK,Plane1} \\ \hat{x}_{ObsK,Plane2} & \hat{y}_{ObsK,Plane2} \end{bmatrix}^{-1} \begin{bmatrix} \hat{z}_{ObsK,Plane1} \\ \hat{z}_{ObsK,Plane2} \end{bmatrix} = \frac{1}{(z_{ObsK} - z)} \begin{bmatrix} (x - x_{ObsK}) \\ (y - y_{ObsK}) \end{bmatrix} \quad (2.18)$$

Which provides two measurements for the K^{th} observer as

$$\begin{bmatrix} \mathsf{y}_{2K-1} \\ \mathsf{y}_{2K} \end{bmatrix} = \frac{1}{(z_{ObsK} - z)} \begin{bmatrix} (x - x_{ObsK}) \\ (y - y_{ObsK}) \end{bmatrix} \tag{2.19}$$

where

$$\begin{bmatrix} \mathsf{y}_{2K-1} \\ \mathsf{y}_{2K} \end{bmatrix} = \begin{bmatrix} \hat{x}_{ObsK,Plane1} & \hat{y}_{ObsK,Plane1} \\ \hat{x}_{ObsK,Plane2} & \hat{y}_{ObsK,Plane2} \end{bmatrix}^{-1} \begin{bmatrix} \hat{z}_{ObsK,Plane1} \\ \hat{z}_{ObsK,Plane2} \end{bmatrix} \tag{2.20}$$

Expanding Equation 2.19 for N observers and replacing $[x \;\; y \;\; z]^T$ with the target position, $\mathbf{R}_{Tar} = [x_{Tar} \;\; y_{Tar} \;\; z_{Tar}]^T$, the measurement model becomes

$$\begin{bmatrix} \mathsf{y}_1 \\ \mathsf{y}_2 \\ \vdots \\ \mathsf{y}_{2N-1} \\ \mathsf{y}_{2N} \end{bmatrix} = \begin{bmatrix} \frac{(x_{Tar} - x_{Obs1})}{(z_{Obs1} - z_{Tar})} \\ \frac{(y_{Tar} - y_{Obs1})}{(z_{Obs1} - z_{Tar})} \\ \vdots \\ \frac{(x_{Tar} - x_{ObsN})}{(z_{ObsN} - z_{Tar})} \\ \frac{(y_{Tar} - y_{ObsN})}{(z_{ObsN} - z_{Tar})} \end{bmatrix} \tag{2.21}$$

Equation 2.21 has the general form of the nonlinear measurement model,

$$\mathbf{y}(t) = \mathbf{h}(\mathbf{x}(t)) \tag{2.22}$$

where $\mathbf{x}(t)$ represents target's unknown state vector. The measurement model in Equation 2.21 can be readily utilized in an extended Kalman filter (EKF) scheme to estimate the inertial position and velocity of the target object as shown in the next section.

Extended Kalman Filter

For the orbit estimation of the target, an extended Kalman filter (EKF) is adopted [37] as shown in Figure 2.6. The target dynamics are assumed to follow the Keplerian two-body motion given in the Cartesian ECI frame by,

$$\dot{\hat{\mathbf{x}}} = \mathbf{f}(\hat{\mathbf{x}}(t)) = \begin{bmatrix} \hat{\mathbf{V}}_{Tar} \\ -\frac{\mu}{\|\hat{\mathbf{R}}_{Tar}\|^3}\hat{\mathbf{R}}_{Tar} \end{bmatrix} \tag{2.23}$$

The Jacobian evaluated at the estimate, $F(\hat{\mathbf{x}})$, is written as,

$$\begin{aligned} F(\hat{\mathbf{x}}(t)) &= \left.\frac{\partial \mathbf{f}}{\partial \mathbf{x}}\right|_{\hat{\mathbf{x}}(t)} \\ &= \begin{bmatrix} 0_{3\times3} & I_{3\times3} \\ F_{21}(\hat{\mathbf{x}}) & 0_{3\times3} \end{bmatrix} \end{aligned} \tag{2.24}$$

where,

$$F_{21}(\hat{\mathbf{x}}) = \frac{\mu}{\|\hat{\mathbf{R}}_{Tar}\|^5} \begin{bmatrix} 3\hat{x}_{Tar}^2 - \|\hat{\mathbf{R}}_{Tar}\|^2 & 3\hat{x}_{Tar}\hat{y}_{Tar} & 3\hat{x}_{Tar}\hat{z}_{Tar} \\ 3\hat{x}_{Tar}\hat{y}_{Tar} & 3\hat{y}_{Tar}^2 - \|\hat{\mathbf{R}}_{Tar}\|^2 & 3\hat{y}_{Tar}\hat{z}_{Tar} \\ 3\hat{x}_{Tar}\hat{z}_{Tar} & 3\hat{y}_{Tar}\hat{z}_{Tar} & 3\hat{z}_{Tar}^2 - \|\hat{\mathbf{R}}_{Tar}\|^2 \end{bmatrix} \tag{2.25}$$

From Equation 2.21, the discretized measurement model at time t_k is,

$$\mathbf{y}_k = \mathbf{h}(\hat{\mathbf{x}}_k) = \begin{bmatrix} \frac{(\hat{x}_{Tar_k} - x_{Obs1_k})}{(z_{Obs1_k} - \hat{z}_{Tar_k})} \\ \frac{(\hat{y}_{Tar_k} - y_{Obs1_k})}{(z_{Obs1_k} - \hat{z}_{Tar_k})} \\ \vdots \\ \frac{(\hat{x}_{Tar_k} - x_{ObsN_k})}{(z_{ObsN_k} - \hat{z}_{Tar_k})} \\ \frac{(\hat{y}_{Tar_k} - y_{ObsN_k})}{(z_{ObsN_k} - \hat{z}_{Tar_k})} \end{bmatrix} \tag{2.26}$$

and the matrix $H(\hat{\mathbf{x}}_k)$ is given by,

$$\begin{aligned} H(\hat{\mathbf{x}}_k) &= \left.\frac{\partial \mathbf{h}}{\partial \mathbf{x}}\right|_{\hat{\mathbf{x}}_k} \\ &= \begin{bmatrix} \frac{1}{(z_{Obs1_k} - \hat{z}_{Tar_k})} & 0 & \frac{(\hat{x}_{Tar_k} - x_{Obs1_k})}{(z_{Obs1_k} - \hat{z}_{Tar_k})^2} & 0 & 0 & 0 \\ 0 & \frac{1}{(z_{Obs1_k} - \hat{z}_{Tar_k})} & \frac{(\hat{y}_{Tar_k} - y_{Obs1_k})}{(z_{Obs1_k} - \hat{z}_{Tar_k})^2} & 0 & 0 & 0 \\ & & \vdots & & & \\ \frac{1}{(z_{ObsN_k} - \hat{z}_{Tar_k})} & 0 & \frac{(\hat{x}_{Tar_k} - x_{ObsN_k})}{(z_{ObsN_k} - \hat{z}_{Tar_k})^2} & 0 & 0 & 0 \\ 0 & \frac{1}{(z_{ObsN_k} - \hat{z}_{Tar_k})} & \frac{(\hat{y}_{Tar_k} - y_{ObsN_k})}{(z_{ObsN_k} - \hat{z}_{Tar_k})^2} & 0 & 0 & 0 \end{bmatrix} \end{aligned} \tag{2.27}$$

The initial state covariance matrix is $P_0^- = \text{diag}(10^8)$. The measurement covariance, R, starts with the standard deviation of the measurement angles, $\sigma_{El} = \sigma_{Az} = 0.03^\circ$. It then undergoes a nonlinear transformation, Equation 2.6, two linear transformations, Equation 2.7 and Equation 2.8, and a final nonlinear transformation shown in Equation 2.20. The details of the measurements covariance transformation are presented in Appendix A. The process noise covariance is $Q = \sigma_w^2 I_{3\text{x}3}$ with the input matrix $G = [0_{3\text{x}3}\ I_{3\text{x}3}]^T$. For the discrete measurements, the time step is $\Delta t = 0.5$ s.

To obtain the initial state estimate, the Herrick-Gibbs method [13] is implemented. The Herrick-Gibbs method uses three sequential position measurements and their time of measurement to ap-

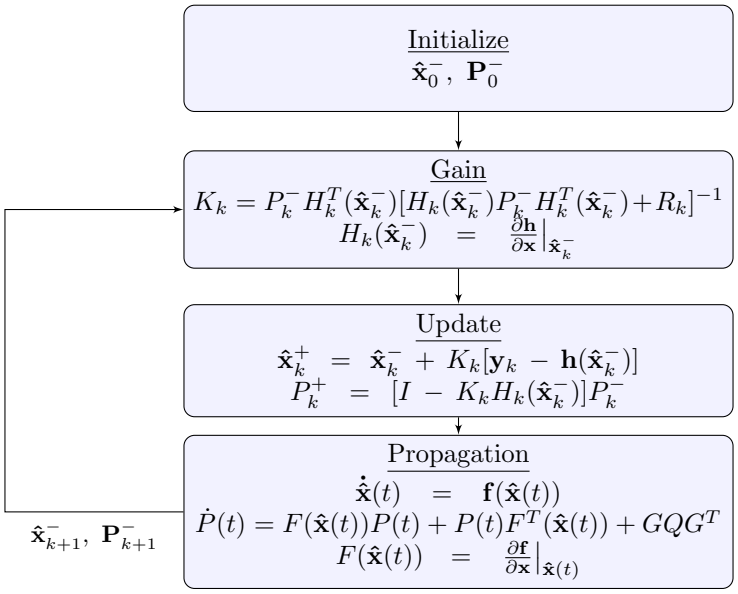

Figure 2.6: Continuous-Discrete Extended Kalman Filter

proximate the velocity at the second measurement. The approximation is done using a Taylor series expansion and works best when each measurement is close together. The first three measurements are used to provide the initial state estimate. This is accomplished by first solving the static position from Equation 2.5.

$$\mathbf{R}_{Tar_i} = (A_i^T A_i)^{-1} A_i^T b_i; \quad \text{For } i = 1,2,3 \tag{2.28}$$

Where,

$$A_i = \begin{bmatrix} \hat{x}_{Obs1,Plane1_i} & \hat{y}_{Obs1,Plane1_i} & \hat{z}_{Obs1,Plane1_i} \\ \hat{x}_{Obs1,Plane2_i} & \hat{y}_{Obs1,Plane2_i} & \hat{z}_{Obs1,Plane2_i} \\ & \vdots & \\ \hat{x}_{ObsN,Plane1_i} & \hat{y}_{ObsN,Plane1_i} & \hat{z}_{ObsN,Plane1_i} \\ \hat{x}_{ObsN,Plane2_i} & \hat{y}_{ObsN,Plane2_i} & \hat{z}_{ObsN,Plane2_i} \end{bmatrix} \tag{2.29}$$

and

$$b_i = \begin{bmatrix} \hat{x}_{Obs1,Plane1_i} x_{Obs1_i} + \hat{y}_{Obs1,Plane1_i} x_{Obs1_i} + \hat{z}_{Obs1,Plane1_i} x_{Obs1_i} \\ \hat{x}_{Obs1,Plane2_i} x_{Obs1_i} + \hat{y}_{Obs1,Plane2_i} x_{Obs1_i} + \hat{z}_{Obs1,Plane2_i} x_{Obs1_i} \\ \vdots \\ \hat{x}_{ObsN,Plane1_i} x_{ObsN_i} + \hat{y}_{ObsN,Plane1_i} x_{ObsN_i} + \hat{z}_{ObsN,Plane1_i} x_{ObsN_i} \\ \hat{x}_{ObsN,Plane2_i} x_{ObsN_i} + \hat{y}_{ObsN,Plane2_i} x_{ObsN_i} + \hat{z}_{ObsN,Plane2_i} x_{ObsN_i} \end{bmatrix} \tag{2.30}$$

Once the three positions are determined, the velocity at the second time instant is determined as,

$$\begin{aligned} \mathbf{V}_{Tar_2} = & -\Delta t_{23} \left(\frac{1}{\Delta t_{12} \Delta t_{13}} + \frac{\mu}{12 \| \mathbf{R}_{Tar_1} \|^3} \right) \mathbf{R}_{Tar_1} \\ & + (\Delta t_{23} - \Delta t_{12}) \left(\frac{\Delta t_{23} + \Delta t_{12}}{\Delta t_{23} \Delta t_{12} \Delta t_{13}} + \frac{\mu}{12 \| \mathbf{R}_{Tar_2} \|^3} \right) \mathbf{R}_{Tar_2} \\ & + \Delta t_{12} \left(\frac{1}{\Delta t_{23} \Delta t_{13}} + \frac{\mu}{12 \| \mathbf{R}_{Tar_3} \|^3} \right) \mathbf{R}_{Tar_3} \end{aligned} \tag{2.31}$$

where

$$\Delta t_{ij} = t_j - t_i \tag{2.32}$$

The initial state estimate becomes $\hat{\mathbf{x}}_0^- = [\mathbf{R}_{Tar_3}\ \mathbf{V}_{Tar_2}]^T$.

Observability Analysis

As discussed in several previous studies [23]–[25], [30], observability plays an important role in measurement models that rely on angles-only. In this section the total system observability and the instantaneous observability of each observer are discussed in order to improve the orbit estimation performance of the present measurement model.

Total Observability

The observability of the system is computed to quantify the performance of the state estimate of the target. For a nonlinear system, the observability gramian [38], [39] is used to measure the sensitivity of the output with respect to the initial conditions. With discrete measurements, the observability gramian is

$$W_d = \sum_{k=0}^{M} \Phi^T(t_k, t_0) H_k^T H_k \Phi(t_k, t_0) \tag{2.33}$$

where M is the total number of discrete measurements and $\Phi(t_k, t_0)$ is the state transition matrix from t_0 to t_k such that,

$$\dot{\Phi}(t_k, t_0) = \left.\frac{\partial \mathbf{f}}{\partial \mathbf{x}}\right|_{\mathbf{x}(t)} \Phi(t_k, t_0) \text{ where } \Phi(t_0, t_0) = I \tag{2.34}$$

To evaluate the observability gramian, the condition number (CN) [40] is utilized. The CN is defined as the ratio of the largest singular value of the observibilty gramian to the smallest, or

$$\mathsf{CN} = \frac{\max \sigma(W_d)}{\min \sigma(W_d)} \tag{2.35}$$

where, σ denotes the singular value. The larger the CN, the greater effect small deviations in initial conditions will have on the final result of the system.

Instantaneous Observability

Because the measurement model, Equation 2.18, requires inverting a matrix, it is important to consider its invertibility at each measurement for each observation node. This can be accomplished by determining the contribution of the observability of each node to the matrix that requires the inversion. Similar to before, the CN is evaluated for the K^{th} observer as,

$$\mathsf{CN}_K = \frac{\max S_K}{\min S_K} \tag{2.36}$$

where,

$$S_K = \sigma\left(\begin{bmatrix} \hat{x}_{ObsK,Plane1} & \hat{y}_{ObsK,Plane1} \\ \hat{x}_{ObsK,Plane2} & \hat{y}_{ObsK,Plane2} \end{bmatrix}\right) \tag{2.37}$$

Also, from Equation 2.18 it can be seen that a singularity forms when the relative z distance goes to zero. As a consequence, the CN is inversely related to the z component of the $\mathbf{L\hat{O}S}$. Through experimentation, it is determined that if $\mathsf{CN}_K > 10^2$ for any observation node, then that particular observer should be excluded for that particular measurement as it has a negative impact on the system as shown in the next section.

CHAPTER 3: NUMERICAL SIMULATIONS

To demonstrate the new measurement model, a series of scenarios are simulated. The first scenario experimentally determines the minimum necessary observation nodes required to accurately track a target. For the second scenario, a formation of four observers are used to track a target. The target dynamics are assumed to be fully known (no process noise) and the formation is designed such that measurements from one of the observers violates the instantaneous observability condition, Equation 2.37. The same experiment is then repeated with the introduction of process noise and the J_2 perturbation in the target true dynamics. Finally, a constellation of observers tracking a single target over an entire orbit period is introduced. Instantaneous observability, range and occlusions caused by Earth are taken into account.

For all simulations, the estimation error, $\mathbf{x}_e$, is calculated as the difference between the true states and the estimated states, $\mathbf{x}_e = \mathbf{x}_k - \hat{\mathbf{x}}_k$. The root mean square (RMS) error is computed in order to measure the total accuracy of the filter as shown in Equation 3.1.

$$RMS = \sqrt{\frac{1}{N}\sum_{1}^{N}\mathbf{x}_e^2} \tag{3.1}$$

Minimum Number of Observation Nodes

Based on the development of nonparallel intersecting planes for the position determination of a static object [36], only two observers are required to generate the needed three planes. To verify the applicability of this approach to a dynamical system via EKF, the number of required observation nodes is validated by considering two, three, and four spacecraft with full observability. The orbit elements for the target and four observation nodes, shown in Table 3.1, were selected so that the

CN is less than the predetermined threshold. Based on the prescribed orbit elements, the average distance between the observation nodes and the target is 62 km. The final time for the scenario is $t_f = 500$ s.

Table 3.1: Orbit elements for the target and observation nodes.

	a (km)	e	i (deg)	Ω (deg)	ω (deg)	M_0 (deg)
Target	8000.0	0	25.0	0	0	80.0
Observer 1	8000.0	0	25.2	0	0	79.6
Observer 2	8000.0	0	25.2	0	0	80.4
Observer 3	8000.0	0	25.4	0	0	79.8
Observer 4	8000.0	0	25.4	0	0	80.2

With all four observation nodes, it can be seen in Figure 3.1 that the position and velocity error is converging toward zero. When only three observers are used, the position and velocity error is similar to that of four observation node, as seen in Figure 3.2. It can be seen that for both four and three observers, the components of the position error converge to within ± 10 m and the components of the position error converge to within ± 0.1 m/s within a very short period of time after the start of the simulation. For only two observation nodes, it can be seen in Figure 3.3 that the position and velocity error converges to zero just as in the case of four and three observers, although this convergence is not quite as fast.

Form Table 3.2, it can be seen that there is a minor improvement in the position error with each additional observation node. It can also be seen that the velocity error only undergoes a minor fluctuation as the number of observation nodes is increased. The condition number remains relatively static regardless of the number of observation nodes. The minor changes in the error between the number of observers show that it is possible to use as few as two nodes if they have full observability.

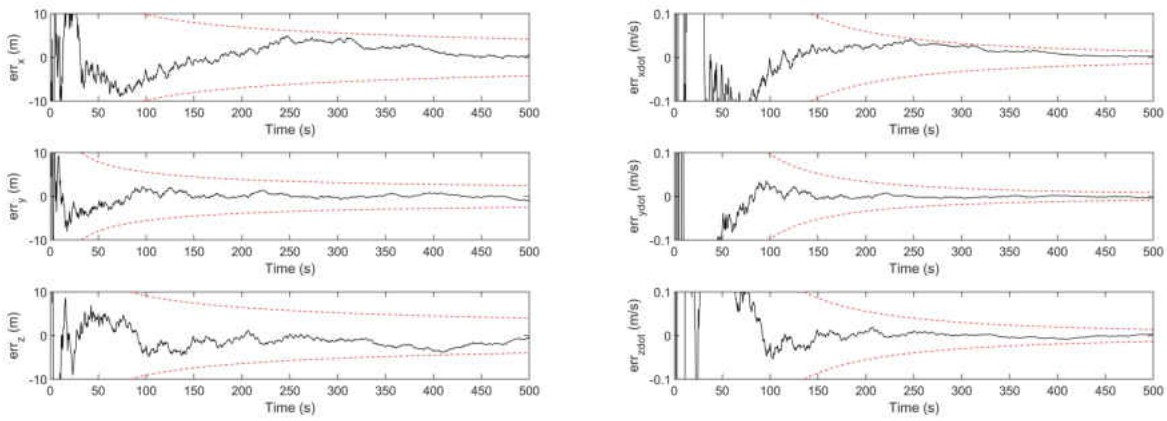

(A) (B)

Figure 3.1: Position (A) and Velocity (B) error (black) and $\mathbf{3}\sigma$ bounds (red) using four observation nodes.

Table 3.2: RMS position and velocity error and condition number

	Number of Observers		
	2	3	4
Position Error (m)	11.232	7.916	6.654
Velocity Error (m/s)	2.960	3.252	2.464
Condition Number	$2.768\text{x}10^6$	$2.521\text{x}10^6$	$2.309\text{x}10^6$

Small Formation Unperturbed Target Dynamics

As discussed in Chapter 2, for continuous tracking, there would be instances where the resulting measurements may have a negative effect on the estimates. This is a result of the matrix inverse operation in the measurement model, Equation 2.18. To remedy this, the condition number is used to evaluate the instantaneous observability as introduced in Equation 2.37. Propagating the orbit elements shown in Table 3.1 with only Keplerian two-body motion for the target and the observers with $\sigma_w = 0$ and $t_f = 1500$ s, the EKF is implemented to estimate the target states using all four

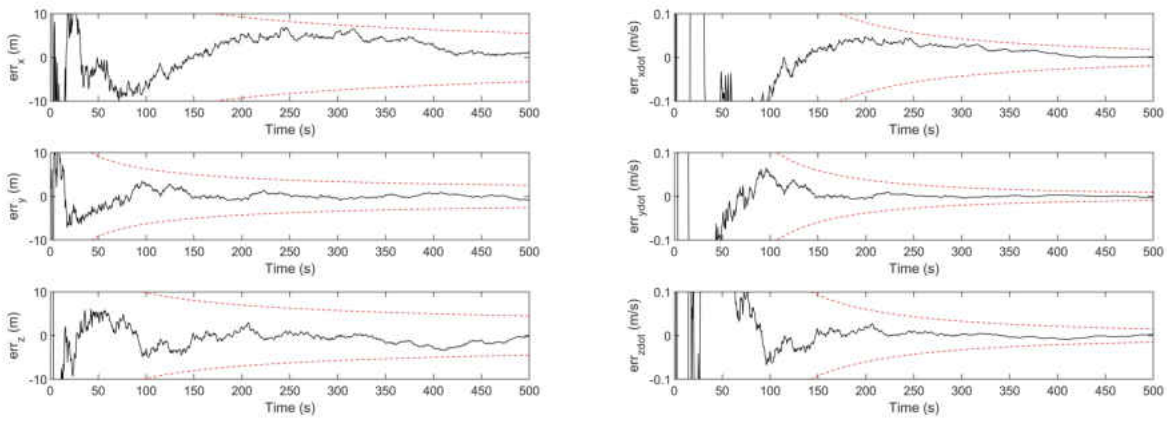

(A) (B)

Figure 3.2: Position (A) and Velocity (B) error (black) and $\mathbf{3}\sigma$ bounds (red) using three observation nodes.

observers.

With all four observation nodes in use, a problem arises when there is an observer with poor observability, in this case Observer 2. This results in poor/divergent performance for the filter as shown in Figure 3.4. The RMS in position and velocity error is 28.292 m and 1.422 m/s, respectively. The resulting condition number for the system is $2.535\text{x}10^{19}$, meaning that it is highly sensitive to measurement noise.

From Figure 3.5A, it can be seen that Observer 2 exceeds the threshold of $\mathsf{CN} = 10^2$ at approximately $t = 1100$ s, which is the same time point at which the estimation begins to diverge. When Observer 2 is prevented from providing measurements whenever the threshold is exceeded, as shown in Figure 3.5B, the distorted measurements will not be included in the Kalman filter. When implemented, the estimation that was originally shown to diverge in Figure 3.4 is now shown to converge in Figure 3.6. The resulting RMS error is found to be 3.926 m for position and 1.422 m/s for velocity. The condition number for the system is found to be $1.901\text{x}10^{11}$, that is 8 orders of

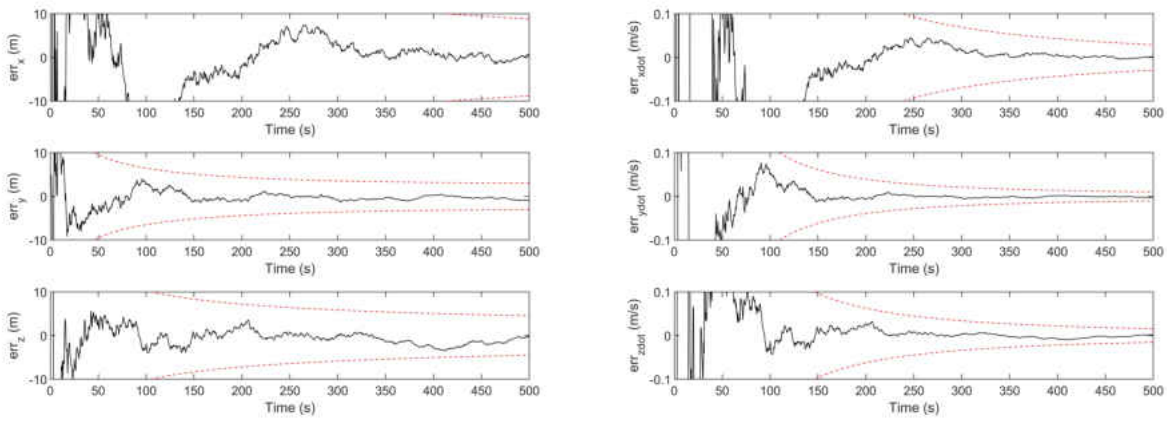

(A) (B)

Figure 3.3: Position (A) and Velocity (B) error (black) and $\mathbf{3}\sigma$ bounds (red) using two observation nodes.

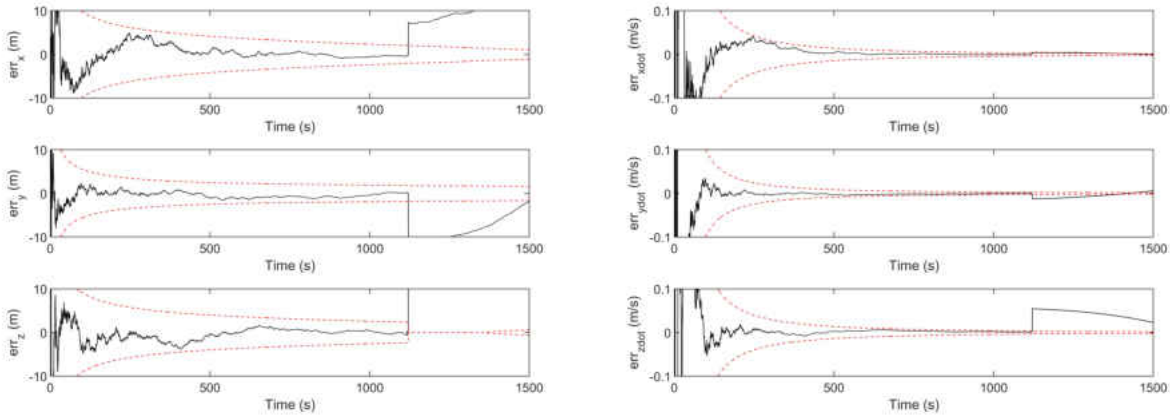

(A) (B)

Figure 3.4: Position (A) and Velocity (B) error (black) and $\mathbf{3}\sigma$ bounds (red) using all available observation nodes.

magnitude improvement over the previous case.

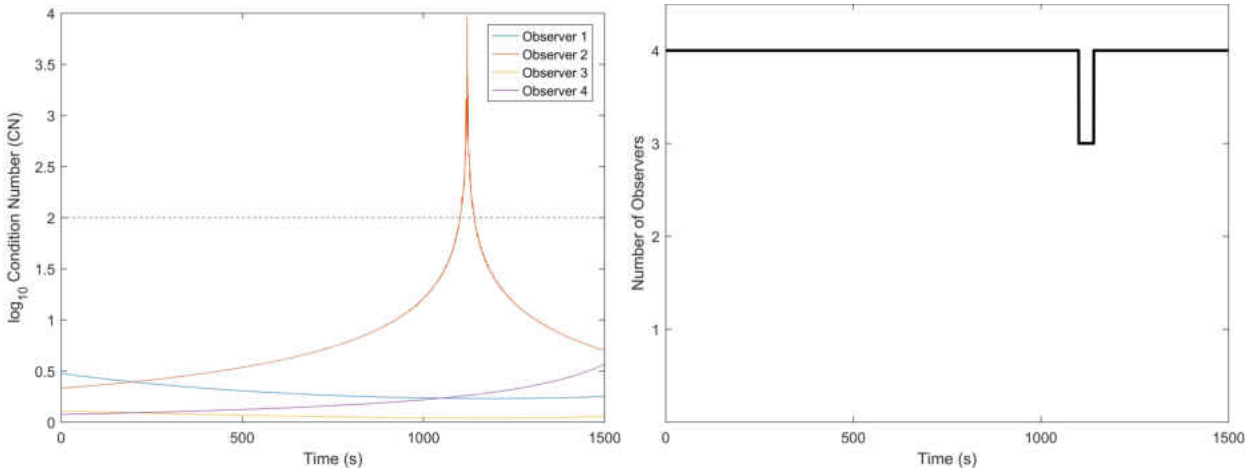

(A) (B)

Figure 3.5: (A) Condition Number for each observation node. (Threshold of $\mathbf{CN} = 10^2$ shown). (B) Number of observation nodes

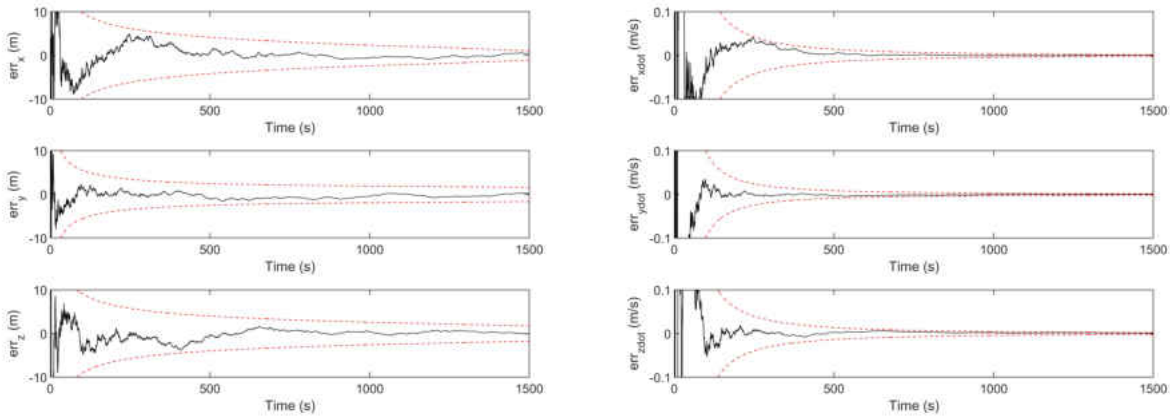

(A) (B)

Figure 3.6: Position (A) and Velocity (B) error (black) and $\mathbf{3}\sigma$ bounds (red) using only select observation nodes.

Small Formation J_2 Perturbed Target Dynamics

The same formation in Table 3.1 is used for the orbit estimation of the target with true dynamics that includes gravity perturbations. The gravity perturbations are modeled by the J_2 (Earth oblateness) effect given by [41]

$$\mathbf{a}_{J_2} = \frac{3}{2} J_2 \frac{\mu}{\|\mathbf{R}_{Tar}\|^3} \left(\frac{R_E}{\|\mathbf{R}_{Tar}\|} \right)^2 \begin{bmatrix} x_{Tar} \left(5 \left(\frac{z_{Tar}}{\|\mathbf{R}_{Tar}\|} \right)^2 - 1 \right) \\ y_{Tar} \left(5 \left(\frac{z_{Tar}}{\|\mathbf{R}_{Tar}\|} \right)^2 - 1 \right) \\ z_{Tar} \left(5 \left(\frac{z_{Tar}}{\|\mathbf{R}_{Tar}\|} \right)^2 - 3 \right) \end{bmatrix} \tag{3.2}$$

where R_E is the equatorial radius of Earth and $J_2 = 1082.63 \times 10^{-6}$. The EKF is implemented with process noise, $\sigma_w = 3\text{x}10^{-2}$, and $t_f = 1500$ s.

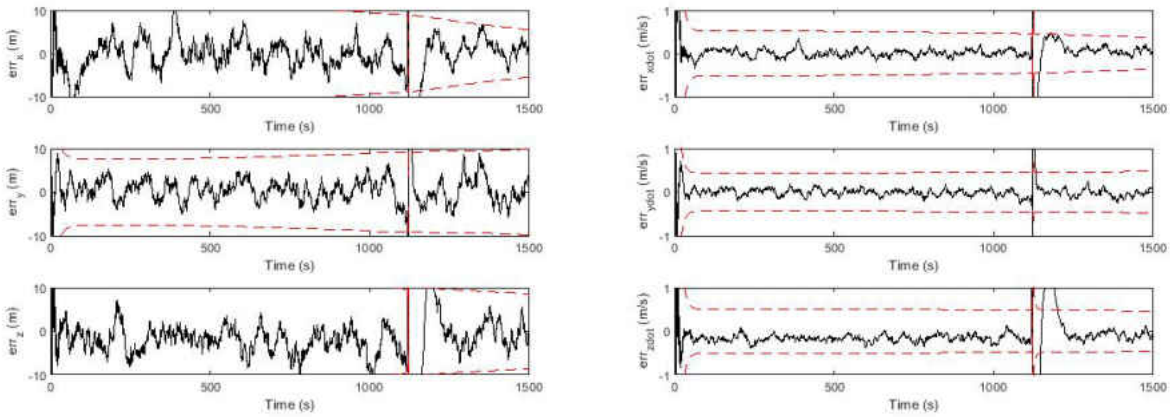

(A) (B)

Figure 3.7: Position (A) and Velocity (B) error (black) and $\mathbf{3\sigma}$ bounds (red) using all available observation nodes with gravity perturbations.

In the case of including measurements from all observers, a problem arises when Observer 2 (with poor observability) is allowed to contribute measurements to the filter. As can be seen in Figure 3.7,

there is an instant when the position and velocity error undergo an extreme increase. With a condition number for the system of $2.135\text{x}10^{16}$, the poor observer made the filter sensitive to measurement noise. As a result, the RMS position error is 150.145 m and the RMS velocity error is 5.419 m/s.

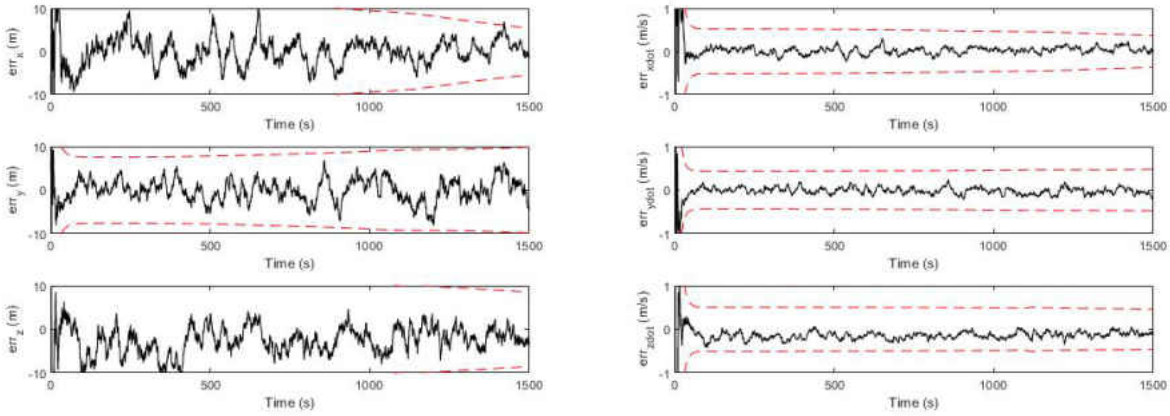

(A) (B)

Figure 3.8: Position (A) and Velocity (B) error (black) and $\mathbf{3}\sigma$ bounds (red) using only select observation nodes with gravity perturbations.

Applying the condition number threshold, Figure 3.8 shows the improved estimates of the target states. Compared to Figure 3.6, the inclusion of process noise resulted in an increase in the noise of the error signal; however, the resulting RMS errors are still in the order of meters. The RMS position error is 6.323 m and an RMS velocity error is 1.433 m/s. The system had a condition number of $1.902\text{x}10^{11}$.

A Large Constellation of Observers

To simulate a more realistic scenario, a constellation of observation satellites is simulated to track a single target throughout a single orbit, Figure 3.9A. Chosen for its simplicity, the Walker Con-

stellation [42] is utilized. The elements of the Walker Constellation are $50^\circ : 1296/36/0$, or 1296 satellites evenly distributed over 36 orbits, all with an inclination angle of 50°. All orbits are circular with a semi-major axis of 6800 km. The target object is in a circular orbit with a semi-major axis of 6750 km, inclination of 28.5°, true anomaly -10°. The argument of perigee and longitude of the ascending node are both 0°. The final time is $t_f = 5500$ s and perturbations are not included with $\sigma_w = 0$.

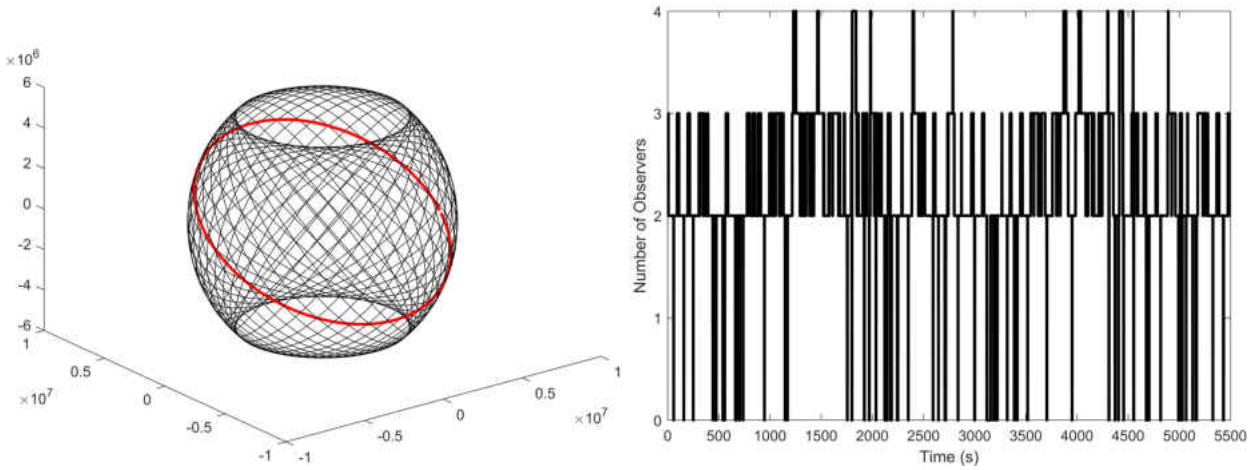

(A) (B)

Figure 3.9: (A) Orbits of the observation satellite constellation (black) and target satellite (red) (B) Number of observation nodes

Each observer is assumed to have a maximum sensor range of 600 km. It is important to verify that the observers view of the target is not obstructed by the Earth. This obstruction occurs if and only if there exists $\alpha \in [0,1]$ such that $D(\alpha) < R_E$ [16]. Where

$$\alpha = -\frac{x_{ObsK}(x_{Tar} - x_{ObsK}) + y_{ObsK}(y_{Tar} - y_{ObsK}) + z_{ObsK}(z_{Tar} - z_{ObsK})}{(x_{Tar} - x_{ObsK})^2 + (y_{Tar} - y_{ObsK})^2 + (z_{Tar} - z_{ObsK})^2} \tag{3.3}$$

and

$$D(\alpha) = \sqrt{(\alpha x_{Tar} + (1-\alpha)x_{ObsK})^2 + (\alpha y_{Tar} + (1-\alpha)y_{ObsK})^2 + (\alpha z_{Tar} + (1-\alpha)z_{ObsK})^2} \quad (3.4)$$

Once the target is in range of the observer and is not obstructed be the Earth, the instantaneous observability check from Chapter 2 is perform to determine if the measurements are suitable for the estimation filter. After checking the instantaneous observability, there were 133 instances where a single observer had to be removed and 18 instances where two observers had to be removed. In the event that only one observer was available, the measurements from that observer were excluded and previous estimate was just propagated to the next time step. Throughout this scenario, the average number of observers used was 2.33 and are shown for each time step in Figure 3.9B.

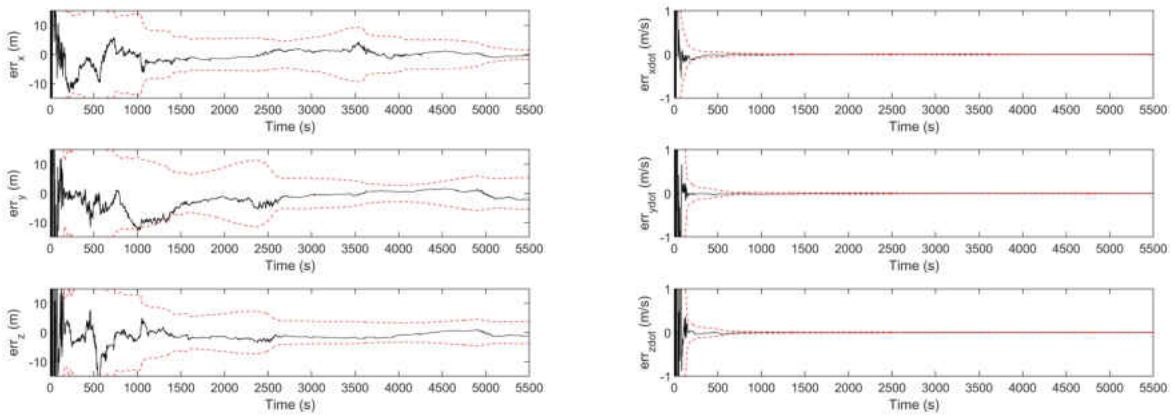

(A) (B)

Figure 3.10: Position (A) and Velocity (B) error (black) and $\mathbf{3}\sigma$ bounds (red) using only select observation nodes from the constellation.

As shown in Figure 3.10, there is minimal position and velocity error as the estimation moves forward in time toward t_f. The resulting RMS position and velocity errors are 24.240 m and

9.343 m/s, respectively. The condition number for the system is $4.106\text{x}10^{10}$.

The overall numerical results are summarized in Table 3.3. In the case of using all observers in a small formation, the estimation error and system condition number are both large when the observability of the observation nodes are not taken into account. For a small formation using only select observers, the results are much more accurate based on the estimation error and system condition number. With the introduction of the gravity perturbations, using all observers in a small formation results in a poor estimation error and condition number due to each observers observability not taken into account. When only select observers in the small formation are utilized and gravity perturbations is included, the estimation error and condition number show that the results are very accurate. The final case shows the a large constellation can accurately track an object throughout its entire orbit.

Table 3.3: Summary of numerical results.

	Sim. Time (s)	Pos. RMS Error (m)	Vel. RMS Error (m/s)	Condition Number
Small Formation; No Process Noise; All Observers	1500	28.292	1.422	$2.535\text{x}10^{19}$
Small Formation; No Process Noise; Select Observers	1500	3.926	1.422	$1.901\text{x}10^{11}$
Small Formation; w/ J_2; All Observers	1500	150.145	5.419	$2.135\text{x}10^{16}$
Small Formnation; w/ J_2; Select Observers	1500	6.323	1.433	$1.902\text{x}10^{11}$
Large Constellation (50° : 1296/36/0)	5500	24.240	9.343	$4.106\text{x}10^{10}$

It is shown that the new measurement model, Equation 2.21, can produce accurate estimates even in the event of poor observability that results in “bad" measurements. In the case of an observation node with poor observability that produces undesirable measurements, the measurement model allows for the measurements of that observation node to be temporarily excluded from the Kalman

filter and for the estimate to maintain its overall accuracy.

CHAPTER 4: CONCLUSION

In this paper, a new measurement model for angles-only line of sight orbit estimation based on multiple observation nodes is presented. It is shown that when the observation nodes have full observability, only a minimum of two are required in order to have an accurate estimation of the position and velocity of a target over a short period of time. It is also shown that there are instances when a particular observation node will have poor instantaneous observability which adversely affects the filter performance. If the observation node were allowed to provide measurement to the Kalman filter, the estimation diverges. However, it is also shown that the measurement model allows for that observation node to be easily excluded from the Kalman filter and have the estimated results remain accurate. This was taken a step further and applied to a large constellation of observation satellites, where the number of observation nodes varied based on range, instantaneous observability and occlusions by Earth. For this study, field of view is not taken into account and is assumed that each observer has a means to orient its sensor toward the target. The orbit estimation results maintained a very high accuracy (an RMS error on the order of meters in position and m/s in velocity).

Future Work

The present measurement model can be readily used to optimize a network of observers for continuous coverage that takes into account the observer orientation. Additionally, the structure of the measurement model lends itself to a decentralized estimation framework. By taking advantage of the ability of the measurement model to be subdivided, decentralizing the computation can replace the need for a centralized computing node and streamline the estimation. The measurement model can also be implemented in a nonlinear least squares method for initial orbit determination (IOD).

The results of the IOD can be compared against the classical methods, e.g. Gauss and Laplace, as well as newer methods, e.g. Gooding and Double-r. All are areas that will be explored in future works.

APPENDIX A: CONVERTED MEASUREMENT COVARIANCE

In this section, the transformation of the covariance of the measurement error is presented. The measurements undergo four transformations. First, a nonlinear transformation from spherical coordinates to Cartesian coordinates. Then, two linear transformations involving coordinate rotations. Finally, a nonlinear transformation, Equation 2.20, to complete the measurement transformation.

Nonlinear Transformation: Spherical to Cartesian Coordinates

The random variable transformation from spherical to Cartesian coordinates has been shown before in several works [43]–[45]. It is presented here for completeness taking into account that the transformation in Equation 2.6 does not involve range information. The spherical coordinates are represented by the two angles, azimuth (Az) and elevation (El), and range. Because the angles are used to create a unit vector, the range is deterministic and is equal to one. Therefore it does not need to be included in the transformation. The conversion of spherical to Cartesian coordinates in the body frame is then

$$\begin{aligned} x^{Body} &= \cos El \sin Az \\ y^{Body} &= \cos El \cos Az \\ z^{Body} &= \sin El \end{aligned} \tag{A.1}$$

The measured angles Az_m, and El_m are

$$\begin{aligned} Az_m &= Az + \tilde{A}z \\ El_m &= El + \tilde{E}l \end{aligned} \tag{A.2}$$

Where $\tilde{Az}$ and $\tilde{El}$ are the measurement errors. The measurement errors are assumed to be independent zero mean Gaussian random variables with a standard deviation of σ_{Az} and σ_{El} for azimuth and elevation, respectively. The error in Cartesian coordinates is expressed as

$$\begin{aligned} \tilde{x}^{Body} &= x_m^{Body} - x^{Body} \\ \tilde{y}^{Body} &= y_m^{Body} - y^{Body} \\ \tilde{z}^{Body} &= z_m^{Body} - z^{Body} \end{aligned} \tag{A.3}$$

where, when including Equation A.1, and Equation A.2, can then be expressed as

$$\begin{aligned} \tilde{x}^{Body} &= \cos(El + \tilde{El})\sin(Az + \tilde{Az}) - \cos El \sin Az \\ \tilde{y}^{Body} &= \cos(El + \tilde{El})\cos(Az + \tilde{Az}) - \cos El \cos Az \\ \tilde{z}^{Body} &= \sin(El + \tilde{El}) - \sin El \end{aligned} \tag{A.4}$$

The mean error is computed using the expected value operator, $E(\cdot)$, as

$$\mu^{Body} = [\mu^x, \mu^y, \mu^z]^T = E([\tilde{x}^{Body}, \tilde{y}^{Body}, \tilde{z}^{Body}]^T \ | Az, El) \tag{A.5}$$

Using the following relations for the expected value of a trigonometric function of a random variable, $\tilde{\theta}$, [44]

$$
\begin{aligned}
E[\sin\tilde{\theta}] &= 0 \\
E[\cos\tilde{\theta}] &= e^{-\frac{\sigma^2}{2}} \\
E[\sin^2\tilde{\theta}] &= \frac{1}{2}\left(1-e^{-2\sigma^2}\right) \\
E[\cos^2\tilde{\theta}] &= \frac{1}{2}\left(1+e^{-2\sigma^2}\right)
\end{aligned}
\tag{A.6}
$$

where σ is the standard deviation of the random variable, the mean error is then

$$
\begin{aligned}
\mu^x &= e^{-\sigma_{El}^2/2-\sigma_{Az}^2/2}\cos El\sin Az - \cos El\sin Az \\
\mu^y &= e^{-\sigma_{El}^2/2-\sigma_{Az}^2/2}\cos El\cos Az - \cos El\cos Az \\
\mu^z &= e^{-\sigma_{El}^2/2}\sin El - \sin El
\end{aligned}
\tag{A.7}
$$

The measurement covariance is then computed as

$$
R^{Body} = \begin{bmatrix} R^{xx} & R^{xy} & R^{xz} \\ R^{yx} & R^{yy} & R^{yz} \\ R^{zx} & R^{zy} & R^{zz} \end{bmatrix} = \mathsf{cov}([\tilde{x}^{Body}, \tilde{y}^{Body}, \tilde{z}^{Body}]^T \mid Az, El) \tag{A.8}
$$

where the covariance of two random variables, $\tilde{X}$ and $\tilde{Y}$ is

$$
R^{XY} = \mathsf{cov}(\tilde{X},\tilde{Y}) = E[\tilde{X}\tilde{Y}] - E[\tilde{X}]E[\tilde{Y}] \tag{A.9}
$$

The elements of the measurement covariance are then given by,

$$
\begin{aligned}
R^{xx} =& \cos^2 Az \sin^2 El \left(\frac{e^{-2\sigma_{El}^2}}{2} - \frac{1}{2}\right)\left(\frac{e^{-2\sigma_{Az}^2}}{2} - \frac{1}{2}\right) \\
&- \cos^2 Az \cos^2 El \left(\frac{e^{-2\sigma_{El}^2}}{2} + \frac{1}{2}\right)\left(\frac{e^{-2\sigma_{Az}^2}}{2} - \frac{1}{2}\right) \\
&+ \sin^2 Az \cos^2 El \left(\frac{e^{-2\sigma_{El}^2}}{2} + \frac{1}{2}\right)\left(\frac{e^{-2\sigma_{Az}^2}}{2} + \frac{1}{2}\right) \\
&- \sin^2 Az \sin^2 El \left(\frac{e^{-2\sigma_{El}^2}}{2} - \frac{1}{2}\right)\left(\frac{e^{-2\sigma_{Az}^2}}{2} + \frac{1}{2}\right) \\
&- \sin^2 Az \cos^2 El e^{-\sigma_{Az}^2 - \sigma_{El}^2} \\
R^{yy} =& \cos^2 Az \cos^2 El \left(\frac{e^{-2\sigma_{El}^2}}{2} + \frac{1}{2}\right)\left(\frac{e^{-2\sigma_{Az}^2}}{2} + \frac{1}{2}\right) \\
&- \cos^2 Az \sin^2 El \left(\frac{e^{-2\sigma_{El}^2}}{2} - \frac{1}{2}\right)\left(\frac{e^{-2\sigma_{Az}^2}}{2} + \frac{1}{2}\right) \\
&- \sin^2 Az \cos^2 El \left(\frac{e^{-2\sigma_{El}^2}}{2} + \frac{1}{2}\right)\left(\frac{e^{-2\sigma_{Az}^2}}{2} - \frac{1}{2}\right) \\
&+ \sin^2 Az \sin^2 El \left(\frac{e^{-2\sigma_{El}^2}}{2} - \frac{1}{2}\right)\left(\frac{e^{-2\sigma_{Az}^2}}{2} - \frac{1}{2}\right) \\
&- \cos^2 Az \cos^2 El e^{-\sigma_{Az}^2 - \sigma_{El}^2} \\
R^{zz} =& \frac{1}{2} e^{-2\sigma_{El}^2}(e^{\sigma_{El}^2} - 1)(\cos 2El + e^{\sigma_{El}^2}) \\
R^{xy} = R^{yx} =& \frac{1}{4}(\sin 2Az\, e^{-2\sigma_{El}^2 - 4\sigma_{Az}^2}\, e^{2\sigma_{El}^2 + 2\sigma_{Az}^2} - e^{\sigma_{El}^2 + 3\sigma_{Az}^2} \\
&- \cos 2El\, e^{\sigma_{El}^2 + 3\sigma_{Az}^2} + \cos 2El\, e^{2\sigma_{Az}^2}) \\
R^{xz} = R^{zx} =& - e^{-2\sigma_{El}^2 - \sigma_{Az}^2/2} \cos El \sin Az \sin El (e^{\sigma_{El}^2} - 1) \\
R^{yz} = R^{zy} =& - e^{-2\sigma_{El}^2 - \sigma_{Az}^2/2} \cos El \cos Az \sin El (e^{\sigma_{El}^2} - 1)
\end{aligned}
\tag{A.10}
$$

Equation A.7 and Equation A.10 are in terms of the true measurements and are therefore impractical to use as the true measurements are not known. Using Equation A.2, the approximated mean

error can be expressed in terms of the measurements as

$$\mu_a^{Body} = [\mu_a^x, \mu_a^y, \mu_a^z]^T = E(\mu^{Body} \mid Az_m, El_m) \tag{A.11}$$

where

$$\begin{aligned}
\mu_a^x &= -\cos El_m \sin Az_m \; e^{-\sigma_{El}^2 - \sigma_{Az}^2}(e^{-\sigma_{El}^2/2 + \sigma_{Az}^2/2} - 1) \\
\mu_a^y &= -\cos El_m \cos Az_m \; e^{-\sigma_{El}^2 - \sigma_{Az}^2}(e^{-\sigma_{El}^2/2 + \sigma_{Az}^2/2} - 1) \\
\mu_a^z &= -\sin El_m \; e^{-\sigma_{El}^2}(e^{-\sigma_{El}^2/2} - 1)
\end{aligned} \tag{A.12}$$

The approximate measurement covariance matrix is

$$R_a^{Body} = \begin{bmatrix} R_a^{xx} & R_a^{xy} & R_a^{xz} \\ R_a^{yx} & R_a^{yy} & R_a^{yz} \\ R_a^{zx} & R_a^{zy} & R_a^{zz} \end{bmatrix} = E(R^{Body} \mid Az_m, El_m) \tag{A.13}$$

where

$$
\begin{aligned}
R_a^{xx} =& \frac{1}{4}\cos 2El_m\ e^{-4\sigma_{El}^2} - \frac{1}{4}\cos 2Az_m\ e^{-4\sigma_{Az}^2} - \frac{1}{4}\ e^{-\sigma_{El}^2}\ e^{-\sigma_{Az}^2} \\
&+ \frac{1}{4}\cos 2Az_m\ e^{-\sigma_{El}^2}\ e^{-3\sigma_{Az}^2} - \frac{1}{4}\cos 2El_m\ e^{-3\sigma_{El}^2}\ e^{-\sigma_{Az}^2} \\
&+ \frac{1}{4}\cos 2Az_m \cos 2El_m\ e^{-3\sigma_{El}^2}\ e^{-3\sigma_{Az}^2} \\
&- \frac{1}{4}\cos 2Az_m \cos 2El_m\ e^{-4\sigma_{El}^2}\ e^{-4\sigma_{Az}^2} + \frac{1}{4} \\
R_a^{yy} =& \frac{1}{4}\cos 2Az_m\ e^{-4\sigma_{Az}^2} + \frac{1}{4}\cos 2El_m\ e^{-4\sigma_{El}^2} - \frac{1}{4}\ e^{-\sigma_{El}^2}\ e^{-\sigma_{Az}^2} \\
&- \frac{1}{4}\cos 2Az_m\ e^{-\sigma_{El}^2}\ e^{-3\sigma_{Az}^2} - \frac{1}{4}\cos 2El_m\ e^{-3\sigma_{El}^2}\ e^{-\sigma_{Az}^2} \\
&- \frac{1}{4}\cos 2Az_m \cos 2El_m\ e^{-3\sigma_{El}^2}\ e^{-3\sigma_{Az}^2} \\
&+ \frac{1}{4}\cos 2Az_m \cos 2El_m\ e^{-4\sigma_{El}^2}\ e^{-4\sigma_{Az}^2} + \frac{1}{4} \\
R_a^{zz} =& \frac{1}{2}\ e^{-4\sigma_{El}^2}(e^{\sigma_{El}^2} - 1)(\cos 2El_m + e^{3\sigma_{El}^2}) \\
R_a^{xy} = R_a^{yx} =& \frac{1}{4}\sin 2Az_m\ e^{-4\sigma_{Az}^2} - \frac{1}{4}\sin 2Az_m\ e^{-\sigma_{El}^2 - 3\sigma_{Az}^2} \\
&- \frac{1}{4}\sin 2Az_m \cos 2El_m\ e^{-3\sigma_{El}^2}\ e^{-3\sigma_{Az}^2} \\
&+ \frac{1}{4}\sin 2Az_m \cos 2El_m\ e^{-4\sigma_{El}^2}\ e^{-4\sigma_{Az}^2} \\
R_a^{xz} = R_a^{zx} =& \cos El_m \sin Az_m \sin El_m (\ e^{-4\sigma_{El}^2}\ e^{-\sigma_{Az}^2} - e^{-3\sigma_{El}^2}\ e^{-\sigma_{Az}^2}) \\
R_a^{yz} = R_a^{zy} =& \cos El_m \cos Az_m \sin El_m (\ e^{-4\sigma_{El}^2}\ e^{-\sigma_{Az}^2} - e^{-3\sigma_{El}^2}\ e^{-\sigma_{Az}^2})
\end{aligned}
\tag{A.14}
$$

Linear Coordinates Transformations

The first linear transformation is a rotation from the body to the LVLH frame. Using the rotation matrix

$$T_{Body\to LVLH} = \begin{bmatrix} 1 & 0 & 0 \\ 0 & \cos\phi & -\sin\phi \\ 0 & \sin\phi & \cos\phi \end{bmatrix} \begin{bmatrix} \cos\theta & 0 & \sin\theta \\ 0 & 1 & 0 \\ -\sin\theta & 0 & \cos\theta \end{bmatrix} \begin{bmatrix} \cos\psi & -\sin\psi & 0 \\ \sin\psi & \cos\psi & 0 \\ 0 & 0 & 1 \end{bmatrix} \tag{A.15}$$

the approximated mean can be transformed by [37]

$$\mu_a^{LVLH} = T_{Body\to LVLH}\,\mu_a^{Body} \tag{A.16}$$

and the approximated measurement covariance can be transformed by

$$R_a^{LVLH} = T_{Body\to LVLH} R_a^{Body} T_{Body\to LVLH}^T \tag{A.17}$$

Similarly, the second linear transformation results from the rotation from the LVLH frame to the ECI frame. The rotation matrix is given by the 3-1-3 Euler angle sequence through the longitude of the ascending node, the inclination angle, and the true longitude.

$$T_{LVLH\to ECI} = \begin{bmatrix} \cos\Theta & -\sin\Theta & 0 \\ \sin\Theta & \cos\Theta & 0 \\ 0 & 0 & 1 \end{bmatrix} \begin{bmatrix} 1 & 0 & 0 \\ 0 & \cos i & -\sin i \\ 0 & \sin i & \cos i \end{bmatrix} \begin{bmatrix} \cos\Omega & -\sin\Omega & 0 \\ \sin\Omega & \cos\Omega & 0 \\ 0 & 0 & 1 \end{bmatrix} \tag{A.18}$$

The approximated mean is transformed by

$$\mu_a^{ECI} = T_{LVLH \to ECI} \mu_a^{LVLH} \tag{A.19}$$

and the approximated measurement covariance is transformed by

$$R_a^{ECI} = T_{LVLH \to ECI} R_a^{LVLH} T_{LVLH \to ECI}^T \tag{A.20}$$

Nonlinear Transformation: Line of Sight Vector

The final transformation is the nonlinear transformation from Equation 2.20 which simplifies to

$$\begin{aligned} \mathsf{y}_1 &= -\frac{x^{ECI}}{z^{ECI}} \\ \mathsf{y}_2 &= -\frac{y^{ECI}}{z^{ECI}} \end{aligned} \tag{A.21}$$

where x^{ECI}, y^{ECI}, and z^{ECI} are components of the line of sight vector in the ECI frame. The measured line of sight vector is then expressed as

$$\begin{aligned} x_m^{ECI} &= x^{ECI} + \tilde{x}^{ECI} \\ y_m^{ECI} &= y^{ECI} + \tilde{y}^{ECI} \\ z_m^{ECI} &= z^{ECI} + \tilde{z}^{ECI} \end{aligned} \tag{A.22}$$

and the measurement error is given by

$$\begin{aligned} \tilde{\mathsf{y}}_1 &= \mathsf{y}_{1_m} - \mathsf{y}_1 \\ \tilde{\mathsf{y}}_2 &= \mathsf{y}_{2_m} - \mathsf{y}_2 \end{aligned} \tag{A.23}$$

Using Equation A.21 and Equation A.22, the measurement error can be expressed as

$$\begin{aligned} \tilde{\mathsf{y}}_1 &= -\frac{\tilde{x}^{ECI}}{z^{ECI}+\tilde{z}^{ECI}} - \frac{x^{ECI}}{z^{ECI}+\tilde{z}^{ECI}} + \frac{x^{ECI}}{z^{ECI}} \\ \tilde{\mathsf{y}}_2 &= -\frac{\tilde{y}^{ECI}}{z^{ECI}+\tilde{z}^{ECI}} - \frac{y^{ECI}}{z^{ECI}+\tilde{z}^{ECI}} + \frac{y^{ECI}}{z^{ECI}} \end{aligned} \tag{A.24}$$

The mean error of the measurements is given by,

$$\mu = [\mu^{\mathsf{y}_1}, \mu^{\mathsf{y}_2}]^T = E([\tilde{\mathsf{y}}_1, \tilde{\mathsf{y}}_2]^T \mid x^{ECI}, y^{ECI}, z^{ECI}) \tag{A.25}$$

Because the measurements involve fractions of random variables, a Taylor series approach [46], [47] is adopted in order to solve for the measurement mean and covariance. The expected value of a fraction of two random variables, X and Y, can be approximated as

$$E\left(\frac{X}{Y}\right) = \frac{E(X)}{E(Y)} - \frac{\mathsf{cov}(X,Y)}{E(Y)^2} + \frac{E(X)\mathsf{var}(Y)}{E(Y)^3} \tag{A.26}$$

and in the case of just a random variable to the negative power

$$E\left(\frac{1}{Y}\right) = \frac{1}{E(Y)} + \frac{\mathsf{var}(Y)}{E(Y)^3} \tag{A.27}$$

From Equation A.26 and Equation A.27, the mean error is expressed as

$$\begin{aligned}
\mu^{\mathsf{y}_1} &= -\left(\frac{x^{ECI}+\mu^x}{z^{ECI}+\mu^z} - \frac{R^{xz}}{(z^{ECI}+\mu^z)^2} + \frac{(x^{ECI}+\mu^x)R^{zz}}{(z^{ECI}+\mu^z)^3}\right) + \frac{x^{ECI}}{z^{ECI}} \\
\mu^{\mathsf{y}_2} &= -\left(\frac{y^{ECI}+\mu^y}{z^{ECI}+\mu^z} - \frac{R^{yz}}{(z^{ECI}+\mu^z)^2} + \frac{(y^{ECI}+\mu^y)R^{zz}}{(z^{ECI}+\mu^z)^3}\right) + \frac{y^{ECI}}{z^{ECI}}
\end{aligned} \tag{A.28}$$

The measurement covariance is

$$R = \begin{bmatrix} R^{\mathsf{y}_1\mathsf{y}_1} & R^{\mathsf{y}_1\mathsf{y}_2} \\ R^{\mathsf{y}_2\mathsf{y}_1} & R^{\mathsf{y}_2\mathsf{y}_2} \end{bmatrix} = \mathsf{cov}([\tilde{\mathsf{y}}_1, \tilde{\mathsf{y}}_2]^T \mid x^{ECI}, y^{ECI}, z^{ECI}) \tag{A.29}$$

Just like in Appendix A.1, the mean error and measurement covariance in Equation A.28 and Equation A.29, respectively, are expressed in terms of the true measurements. Using Equation A.22, the mean error and measurement covariance can be approximated as

$$\mu_a = [\mu_a^{\mathsf{y}_1}, \mu_a^{\mathsf{y}_2}]^T = E([\mu^{\mathsf{y}_1}, \mu^{\mathsf{y}_2}]^T \mid x_m^{ECI}, y_m^{ECI}, z_m^{ECI}) \tag{A.30}$$

and

$$R_a = \begin{bmatrix} R_a^{\mathsf{y}_1\mathsf{y}_1} & R_a^{\mathsf{y}_1\mathsf{y}_2} \\ R_a^{\mathsf{y}_2\mathsf{y}_1} & R_a^{\mathsf{y}_2\mathsf{y}_2} \end{bmatrix} = E(R \mid x_m^{ECI}, y_m^{ECI}, z_m^{ECI}) \tag{A.31}$$

, respectively.

To obtain the final analytical expressions for the measurement covariance, Equation A.29, the approximate mean error, Equation A.30, and approximate measurement covariance, Equation A.31, a symbolic manipulator was used. Due to the size of the resulting equations, they are not presented here and can be provided by contacting the author.

LIST OF REFERENCES

[1] D. Zimpfer, P. Kachmar, and S. Tuohy, "Autonomous rendezvous, capture and in-space assembly: Past, present and future," in *1st Space exploration conference: continuing the voyage of discovery*, 2005, p. 2523.

[2] B. Sherwood, D. B. Smith, R. Greeley, W. Whittaker, G. R. Woodcock, G. Barton, D. W. Pearson, and W. Siegfried, "Mars sample return: Architecture and mission design," in *Proceedings, IEEE Aerospace Conference*, IEEE, vol. 2, 2002, pp. 2–536.

[3] L. Tarabini, J. Gil, F. Gandia, M. Á. Molina, J. M. Del Cura, and G. Ortega, "Ground guided CX-OLEV rendez-vous with uncooperative geostationary satellite," *Acta Astronautica*, vol. 61, no. 1-6, pp. 312–325, 2007.

[4] W. H. Blume, "Deep impact: Mission design approach for a new discovery mission," *Acta Astronautica*, vol. 52, no. 2-6, pp. 105–110, 2003.

[5] P. D. Anz-Meador, "Orbital debris quarterly news volume 23, issues 1 & 2," 2019.

[6] D. J. Kessler, N. L. Johnson, J. Liou, and M. Matney, "The Kessler syndrome: Implications to future space operations," *Advances in the Astronautical Sciences*, vol. 137, no. 8, p. 2010, 2010.

[7] Interagency working group for detecting and mitigating the impact of Earth-bound near-Earth objects, "National near-earth object preparedness strategy," National Science and Technology Council, Tech. Rep., 2018.

[8] J. D. Anderson, "Theory of orbit determination. part i: Classical methods," Jet Propulsion Laboratory, Tech. Rep. 32-497, 1963.

[9] R. L. Branham, "Laplacian orbit determination and differential corrections," *Celestial Mechanics and Dynamical Astronomy*, vol. 93, no. 1-4, pp. 53–68, 2005.

[10] P. R. Escobal, "Methods of orbit determination," *New York: Wiley, 1965*, 1965.

[11] R. Gooding, "A new procedure for the solution of the classical problem of minimal orbit determination from three lines of sight," *Celestial Mechanics and Dynamical Astronomy*, vol. 66, no. 4, pp. 387–423, 1996.

[12] R. R. Karimi and D. Mortari, "A performance based comparison of angle-only initial orbit determination methods," *Advances in Astronautical Sciences, AAS/AIAA, Hilton Head Island, South Carolina*, vol. 150, pp. 1793–1809, 2013.

[13] D. A. Vallado, *Fundamentals of astrodynamics and applications*. Springer Science & Business Media, 2001, vol. 12.

[14] J. FOWLER and J. LEE, "An extended Kalman filter in a dynamic spherical coordinate (dysc) system for space based satellite tracking," in *23rd Aerospace Sciences Meeting*, 1985, p. 289.

[15] J. Raol and N. Sinha, "On the orbit determination problem," *IEEE Transactions on Aerospace and Electronic Systems*, no. 3, pp. 274–291, 1985.

[16] B. O. Teixeira, M. A. Santillo, R. S. Erwin, and D. S. Bernstein, "Spacecraft tracking using sampled-data Kalman filters," *IEEE Control Systems Magazine*, vol. 28, no. 4, pp. 78–94, 2008.

[17] H. Chen, G. Chen, E. Blasch, and K. Pham, "Comparison of several space target tracking filters," in *Sensors and Systems for Space Applications III*, International Society for Optics and Photonics, vol. 7330, 2009, p. 73300I.

[18] J. R. Vetter, "Fifty years of orbit determination," *Johns Hopkins APL technical digest*, vol. 27, no. 3, p. 239, 2007.

[19] R. Opromolla, G. Fasano, G. Rufino, and M. Grassi, "Uncooperative pose estimation with a lidar-based system," *Acta Astronautica*, vol. 110, pp. 287–297, 2015.

[20] M. Quinn, V. Jukna, T. Ebisuzaki, I. Dicaire, R. Soulard, L. Summerer, A. Couairon, and G. Mourou, "Space-based application of the can laser to lidar and orbital debris remediation," *The European Physical Journal Special Topics*, vol. 224, no. 13, pp. 2645–2655, 2015.

[21] Y. Wang and Q. Wang, "The application of lidar in detecting space debris," in *2008 International Conference on Optical Instruments and Technology: Optoelectronic Measurement Technology and Applications*, International Society for Optics and Photonics, vol. 7160, 2009, 71601S.

[22] W. Y. W. Qianqian, "The application of lidar in detecting the space debris," in *Proc. of SPIE Vol*, vol. 7160, 2009, 71601S–1.

[23] E. A. Butcher, J. Wang, and T. A. Lovell, "On Kalman filtering and observability in nonlinear sequential relative orbit estimation," *Journal of Guidance, Control, and Dynamics*, vol. 40, no. 9, pp. 2167–2182, 2017.

[24] E. Kaufman, T. A. Lovell, and T. Lee, "Nonlinear observability for relative orbit determination with angles-only measurements," *The Journal of the Astronautical Sciences*, vol. 63, no. 1, pp. 60–80, 2016.

[25] J. Sullivan, A. Koenig, and S. D'Amico, "Improved maneuver-free approach to angles-only navigation for space rendezvous," in *26th AAS/AIAA Space Flight Mechanics Meeting, Napa, CA*, 2016.

[26] D. C. Woffinden and D. K. Geller, "Optimal orbital rendezvous maneuvering for angles-only navigation," *Journal of guidance, control, and dynamics*, vol. 32, no. 4, pp. 1382–1387, 2009.

[27] J. Sullivan and S. D'Amico, "Adaptive filtering for maneuver-free angles-only navigation in eccentric orbits," in *27th AAS/AIAA Space Flight Mechanics Conference*, 2017.

[28] J. Grzymisch and W. Fichter, "Analytic optimal observability maneuvers for in-orbit bearings-only rendezvous," *Journal of Guidance, Control, and Dynamics*, vol. 37, no. 5, pp. 1658–1664, 2014.

[29] F. J. Franquiz, J. D. Muñoz, B. Udrea, and M. J. Balas, "Optimal range observability maneuvers of a spacecraft formation using angles-only navigation," *Acta Astronautica*, vol. 153, pp. 337–348, 2018.

[30] D. C. Woffinden and D. K. Geller, "Observability criteria for angles-only navigation," *IEEE Transactions on Aerospace and Electronic Systems*, vol. 45, no. 3, pp. 1194–1208, 2009.

[31] D. K. Geller and I. Klein, "Angles-only navigation state observability during orbital proximity operations," *Journal of Guidance, Control, and Dynamics*, vol. 37, no. 6, pp. 1976–1983, 2014.

[32] T. Chen and S. Xu, "Double line-of-sight measuring relative navigation for spacecraft autonomous rendezvous," *Acta Astronautica*, vol. 67, no. 1-2, pp. 122–134, 2010.

[33] K. Wang, T. Chen, and S.-J. Xu, "A method of double line-of-sight measurement relative navigation," *Acta Aeronautica et Aeronautica Sinica*, vol. 32, no. 6, pp. 1084–1091, 2011.

[34] H. Wang, X. Zhang, Q. Zhou, and Y. Li, "Autonomous navigation of non-cooperative target based on multiple line-of-sight," in *2017 36th Chinese Control Conference (CCC)*, IEEE, 2017, pp. 6276–6280.

[35] Z. Li, Y. Wang, and W. Zheng, "Space-based optical observations on space debris via multipoint of view," *International Journal of Aerospace Engineering*, vol. 2020, 2020.

[36] W. Gellert, S. Gottwald, M. Hellwich, H. Kästner, and H. Küstner, "Analytic geometry of space," in *The VNR Concise Encyclopedia of Mathematics*, W. Gellert, S. Gottwald, M. Hellwich, H. Kästner, and H. Küstner, Eds. Dordrecht: Springer Netherlands, 1975, pp. 530–

547, ISBN: 978-94-011-6982-0. DOI: 10.1007/978-94-011-6982-0_25. [Online]. Available: https://doi.org/10.1007/978-94-011-6982-0_25.

[37] J. L. Crassidis and J. L. Junkins, "Optimal estimation of dynamic systems," in. Chapman and Hall/CRC, 2011, pp. 184–189.

[38] A. J. Krener and K. Ide, "Measures of unobservability," in *Proceedings of the 48h IEEE Conference on Decision and Control (CDC) held jointly with 2009 28th Chinese Control Conference*, IEEE, 2009, pp. 6401–6406.

[39] U. Vaidya, "Observability gramian for nonlinear systems," in *2007 46th IEEE Conference on Decision and Control*, IEEE, 2007, pp. 3357–3362.

[40] D. Dochain, N. Tali-Maamar, and J. Babary, "On modelling, monitoring and control of fixed bed bioreactors," *Computers and Chemical Engineering*, vol. 11, no. 21, pp. 1255–1266, 1997.

[41] J. L. Junkins and H. Schaub, *Analytical mechanics of space systems*. American Institute of Aeronautics and Astronautics, 2009.

[42] J. G. Walker, "Satellite constellations," *Journal of the British Interplanetary Society*, vol. 37, pp. 559–572, 1984.

[43] D. Lerro and Y. Bar-Shalom, "Tracking with debiased consistent converted measurements versus EKF," *IEEE transactions on aerospace and electronic systems*, vol. 29, no. 3, pp. 1015–1022, 1993.

[44] P. Suchomski, "Explicit expressions for debiased statistics of 3D converted measurements," *IEEE Transactions on Aerospace and Electronic Systems*, vol. 35, no. 1, pp. 368–370, 1999.

[45] M. Longbin, S. Xiaoquan, Z. Yiyu, S. Z. Kang, and Y. Bar-Shalom, "Unbiased converted measurements for tracking," *IEEE Transactions on Aerospace and Electronic Systems*, vol. 34, no. 3, pp. 1023–1027, 1998.

[46] A. Stuart and K. Ord, *Kendall's advanced theory of statistics arnold*, 1994.

[47] R. C. Elandt-Johnson and N. L. Johnson, *Survival models and data analysis*. John Wiley & Sons, 1980, vol. 110, pp. 69–72.